



# Ram Pressure Stripping in the EAGLE Simulation

Andrea Kulier<sup>1</sup>, Bianca Poggianti<sup>1</sup>, Stephanie Tonnesen<sup>2</sup>, Rory Smith<sup>3</sup>, Alessandro Ignesti<sup>1</sup>, Nina Akerman<sup>1,4</sup>,  
Antonino Marasco<sup>1</sup>, Benedetta Vulcani<sup>1</sup>, Alessia Moretti<sup>1</sup>, and Anna Wolter<sup>5</sup>

<sup>1</sup> INAF-Osservatorio Astronomico di Padova, Vicolo dell'Osservatorio 5, I-35122 Padova, Italy; [andrea.kulier@inaf.it](mailto:andrea.kulier@inaf.it)

<sup>2</sup> Flatiron Institute, CCA, 162 5th Avenue, New York, NY 10010, USA

<sup>3</sup> Departamento de Física, Universidad Técnica Federico Santa María, Avenida Vicuña Mackenna 3939, San Joaquín, Santiago, Chile

<sup>4</sup> Dipartimento di Fisica e Astronomia "Galileo Galilei," Università di Padova, Vicolo dell'Osservatorio 3, I-35122 Padova, Italy

<sup>5</sup> INAF-Osservatorio Astronomico di Brera, via Brera 28, I-20121 Milano, Italy

Received 2023 May 8; revised 2023 July 18; accepted 2023 August 5; published 2023 September 6

## Abstract

Ram pressure stripping of satellite galaxies is thought to be a ubiquitous process in galaxy clusters, and a growing number of observations reveal satellites at different stages of stripping. However, in order to determine the fate of any individual galaxy, we turn to predictions from either simulations or analytic models. It is not well determined whether simulations and analytic models agree in their predictions, nor the causes of disagreement. Here we investigate ram pressure stripping in the reference EAGLE hydrodynamical cosmological simulation, and compare the results to predictions from analytic models. We track the evolution of galaxies with stellar mass  $M_* > 10^9 M_\odot$  and initial bound gas mass  $M_{\text{gas}} > 10^9 M_\odot$  that fall into galaxy clusters ( $M_{200c} > 10^{14} M_\odot$ ) between  $z = 0.27$  and  $z = 0$ . We divide each galaxy into its neutral gas disk and hot ionized gas halo and compare the evolution of the stripped gas fraction in the simulation to that predicted by analytic formulations for the two gas phases, as well as to a toy model that computes the motions of gas particles under the combined effects of gravity and a spatially uniform ram pressure. We find that the analytic models generally underpredict the stripping rate of neutral gas and overpredict that of ionized gas, with significant scatter between the model and simulation stripping timescales. This is due to opposing physical effects: the enhancement of ram pressure stripping by stellar feedback, and the suppression of stripping by the compaction of galactic gas.

*Unified Astronomy Thesaurus concepts:* Galaxy evolution (594); Galaxy physics (612); Galaxy structure (622); Hydrodynamical simulations (767); Ram pressure stripped tails (2126)

## 1. Introduction

For decades, it has been known that galaxies in dense regions, such as galaxy clusters and groups, are more likely to be gas-poor and passive than galaxies of the same stellar mass in the field (Dressler 1980). This difference is attributed to a number of physical processes prevalent in such regions, including tidal interactions of satellite galaxies both with other satellites and with the central cluster potential (Byrd & Valtonen 1990; Moore et al. 1996), as well as ram pressure stripping: the removal of gas from satellite galaxies due to the pressure created by their motion relative to the intragroup or intracluster medium (ICM; Gunn et al. 1972). Unlike gravitational interactions, ram pressure acts only on the galactic gas, not on the stars. The most visually spectacular examples of ram pressure stripping are so-called “jellyfish” galaxies, which have undisrupted stellar disks but long, filamentary gaseous tails (Poggianti et al. 2019).

An analytic theoretical treatment of the physics of ram pressure stripping was first provided by Gunn et al. (1972). Such idealized analytic approximations are often used to estimate the stripping rate due to ram pressure, but their assumptions may not be satisfied for real galaxies. Physical effects that are not captured by such simplified treatments have been studied using hydrodynamical simulations. For example, high-resolution simulations of individual galaxies in an

oncoming gas flow have shown that some regions of galactic gas can be shielded from ram pressure by other regions (Roediger & Brüggén 2007; Jáchym et al. 2009). Such simulations have also found that ram pressure can induce spiral waves in the gas that transport angular momentum outward, leading to the contraction of the inner part of the galaxy and preventing further stripping (Schulz & Struck 2001). The strength of both of these effects depends on the orientation of the gas disk relative to the ram pressure direction.

In addition to the HI and molecular gas in the disk, ram pressure can also remove a galaxy’s hot ionized gas halo (i.e., its circumgalactic medium), depriving the galaxy of its source of accreting gas—a process known as “strangulation” (Larson et al. 1980). Simulations have found that the ionized halo can be stripped by modest ram pressures, significantly less than what is required to strip the disk (Bekki et al. 2002; McCarthy et al. 2008; Bekki 2009; Steinhauser et al. 2016).

While high-resolution simulations of individual galaxies allow for investigation of physical processes that cannot be captured by lower-resolution simulations, they also tend to assume idealized initial conditions for the geometry of galaxies and the flow of the ICM. For example, Tonnesen (2019) found that a varying ram pressure produces a different stripping rate than the constant one assumed by many high-resolution simulations.

Cosmological hydrodynamical simulations such as EAGLE (Schaye et al. 2015) and IllustrisTNG (Pillepich et al. 2018) include a wide range of galaxy morphologies that fall into dense regions such as groups and clusters. Due to the cosmological nature of the simulation, these galaxies should



Original content from this work may be used under the terms of the [Creative Commons Attribution 4.0 licence](https://creativecommons.org/licenses/by/4.0/). Any further distribution of this work must maintain attribution to the author(s) and the title of the work, journal citation and DOI.

be statistically representative of the true variety of galaxies that experience ram pressure. Galaxies also experience a range of ram pressures as they traverse different environments. However, due to the lower resolution of these simulations, it is possible that some relevant gas physics is not properly accounted for, such as the influence of magnetic fields (Ramos-Martínez et al. 2018), or the mixing between the interstellar medium and the ICM (Franchetto et al. 2021; Tonnesen & Bryan 2021).

Cosmological hydrodynamical simulations have previously been used to examine a number of aspects of ram pressure stripping. In GIMIC (Crain et al. 2009), a set of simulations of  $\sim 20h^{-1}$  Mpc regions, it was found that stellar feedback enhances the stripping due to ram pressure (Bahé & McCarthy 2015), while confinement pressure has little effect on it (Bahé et al. 2012). Marasco et al. (2016) found that in the EAGLE reference simulation at  $z=0$ , ram pressure stripping was a more common HI gas removal mechanism acting on galaxies than tidal interactions. More recently, Pallero et al. (2022) found that in the C-EAGLE simulations (Barnes et al. 2017), a set of resimulations of galaxy clusters using EAGLE physics, the majority of galaxies that entered the virial radius of a cluster became quenched within 1 Gyr, which the authors attribute to ram pressure stripping, in agreement with a prior cosmological simulation of a single cluster (Tonnesen et al. 2007).

In the Illustris TNG100 simulation, Yun et al. (2019) examined visually identified jellyfish galaxies and found that they had higher Mach numbers and were experiencing higher ram pressures than other galaxies in groups and clusters. They also found that most jellyfish galaxies were recent infallers, having entered the cluster virial radius within the previous 3 Gyr. Rohr et al. (2023) studied jellyfish galaxies in the higher-resolution TNG50 simulation that had been visually identified as part of the Galaxy Zoo project (Zinger et al. 2023). They similarly found that ram pressure stripping of these galaxies begins within approximately 1 Gyr of cluster infall and lasts for  $\lesssim 2$  Gyr, and that the majority of stripping occurs between 0.2 and 2 times the cluster virial radius.

Although both high-resolution and cosmological simulations have been used to theoretically investigate the evolution of ram pressure stripped galaxies, simplified analytic models like the one presented in Gunn et al. (1972) are still frequently used to estimate the effect of ram pressure stripping in the literature—for example, in semianalytic models of galaxy evolution (e.g., Ayromlou et al. 2019; Hough et al. 2023). In this paper, we attempt to assess the differences between the fraction of stripped gas predicted by these models and the results of a full hydrodynamical cosmological simulation, and to analyze the physical effects missing from the analytic models that give rise to these differences.

Specifically, we use the  $(100 \text{ Mpc})^3$  reference EAGLE cosmological hydrodynamical simulation, in which we select galaxies with stellar masses  $M_* > 10^9 M_\odot$  and initial bound gas masses of  $M_{\text{gas}} > 10^9 M_\odot$  that fall into galaxy clusters between the simulation snapshots at  $z = 0.27$  and  $z = 0$ , i.e., within the last 3.2 Gyr. We compare the stripped gas mass in the simulation to that predicted by common analytic prescriptions, and use the differences between the two to determine the additional physical processes that impact the amount of gas stripped by ram pressure. To assist in doing the latter, we implement an additional toy model of greater complexity than

the analytic models. This model integrates the motion of the gas particles within the gravitational potential of each subhalo, using the starting positions and velocities of the gas particles as initial conditions. By comparing this model to both the simulation and simple analytic models, we are able to separate the different physical effects that influence the ram pressure stripping rate of simulated galaxies.

In Section 2, we provide a brief overview of the EAGLE simulation and describe the sample of simulated galaxies used in our analysis. In Section 3, we describe the simplified models to which we compare the results of the simulation. In Section 4, we present our results comparing the analytic models for ram pressure stripping, our more complex toy model, and the EAGLE simulation. In Section 5, we utilize our toy model to explain the physical effects that give rise to most of the discrepancies between the analytic models and the simulation. Finally, in Section 6, we summarize our conclusions.

## 2. Simulations and Galaxy Sample

### 2.1. EAGLE Simulation Overview

EAGLE (Crain et al. 2015; Schaye et al. 2015; McAlpine et al. 2016) is a suite of cosmological hydrodynamical simulations, run using a modified version (Schaller et al. 2015) of the  $N$ -body smoothed particle hydrodynamics (SPH) code GADGET-3 (Springel 2005). These modifications are based on the conservative pressure-entropy formulation of SPH from Hopkins (2013), and include changes to the handling of the viscosity (Cullen & Dehnen 2010), the conduction (Price 2008), the smoothing kernel (Dehnen & Aly 2012), and the time-stepping (Durier & Dalla Vecchia 2012). EAGLE adopts a Planck cosmology (Planck Collaboration et al. 2014) with  $h = 0.6777$ ,  $\Omega_\Lambda = 0.693$ ,  $\Omega_m = 0.307$ , and  $\Omega_b = 0.048$ , which we also adopt throughout this paper.

In this paper, we use the reference EAGLE simulation Ref-L0100N1504, which has a box size of 100 comoving Mpc per side and contains  $1504^3$  particles each of dark matter and baryons. The dark matter particle mass is  $9.70 \times 10^6 M_\odot$  and the initial gas (baryon) particle mass is  $1.81 \times 10^6 M_\odot$ . The Plummer-equivalent gravitational softening length is 2.66 comoving kpc until  $z = 2.8$  and 0.70 proper kpc afterward. Every particle in EAGLE, whether dark matter or baryonic, has a unique identifier that allows it to be tracked throughout the simulation at different times.

The subgrid physics in EAGLE includes prescriptions for radiative cooling, photoionization heating, star formation, stellar mass loss, stellar feedback, supermassive black hole accretion and mergers, and active galactic nucleus (AGN) feedback. These prescriptions and the effects of varying them are described in Schaye et al. (2015) and Crain et al. (2015).

Radiative cooling and photoionization heating are implemented using the model of Wiersma et al. (2009a). Cooling and heating rates are computed for 11 elements using CLOUDY (Ferland et al. 1998), assuming that the gas is optically thin, in ionization equilibrium, and exposed to the cosmic microwave background and a Haardt & Madau (2001) UV and X-ray background.

Star formation is implemented as described in Schaye & Dalla Vecchia (2008). Gas particles that reach a metallicity-dependent density threshold (Schaye 2004) become “star-forming” and are stochastically converted into stars at a rate that reproduces the Kennicutt–Schmidt law

(Kennicutt 1998). Star particles are modeled as simple stellar populations with a Chabrier (2003) initial mass function. Prescriptions for stellar evolution and mass loss from Wiersma et al. (2009b) are used.

Stellar feedback is modeled using the stochastic, purely thermal feedback prescription of Dalla Vecchia & Schaye (2012). When a newly formed star particle reaches an age of 30 Myr, it injects feedback energy into its surroundings by heating some number of neighboring gas particles by  $10^{7.5}$  K. The total injected energy is calibrated by adjusting the fraction of total stellar feedback energy that heats the nearby gas. Stellar feedback in the EAGLE reference simulation was calibrated to simultaneously reproduce the local galaxy stellar mass function and mass–size relation (Crain et al. 2015).

When a dark matter halo reaches a mass of  $10^{10} M_{\odot}/h$ , it is seeded with a black hole of subgrid mass  $10^5 M_{\odot}/h$  at its center by converting the most bound gas particle into a “black hole” particle (Springel et al. 2005). The black hole particles accrete gas according to the modified Bondi–Hoyle prescription given in Rosas-Guevara et al. (2016), and can merge with one another. AGN feedback is implemented as stochastic and purely thermal, similar to stellar feedback. The energy injection rate is proportional to the black hole accretion rate. Gas particles near the black hole particle are stochastically heated by  $10^{8.5}$  K. The fraction of lost energy that is assumed to heat the gas does not significantly affect the masses of galaxies due to self-regulation (Booth & Schaye 2010), and is instead calibrated to match the observed stellar mass–black hole mass relation.

Galaxies are identified in EAGLE through a series of steps. First, halos are identified in the dark matter particle distribution using a friends-of-friends (FoF) algorithm with a linking length of  $b = 0.2$  times the mean interparticle separation (Davis et al. 1985). Other particle types (gas, stars, and black holes) are assigned to the FoF halo of the nearest dark matter particle. The SUBFIND (Springel et al. 2001; Dolag et al. 2009) algorithm is then run over all of the particles of any type within each FoF halo, in order to identify local overdensities (“subhalos”). Each subhalo is assigned only the particles gravitationally bound to it, with no overlap in particles between subhalos. The subhalo that contains the most bound particle in an FoF halo is considered to be the “central” subhalo, while any other subhalos are “satellites.” The gravitationally bound gas and star particles in each subhalo constitute a “galaxy.”

As we will describe below, we track galaxies between  $z = 0.27$  and  $z = 0$ , between which there are 28 short-timescale simulation outputs (termed “snipshots”) that have been processed with SUBFIND. These outputs are generally spaced by  $\approx 120$  Myr: in 25 cases, they are spaced by between 119 and 128 Myr, while two cases are spaced by 59 and 61 Myr, respectively. The snipshots are useful for studying physical processes that can be rapid, such as ram pressure stripping.

Galaxy merger trees were created using the D-TREES algorithm (Jiang et al. 2014) as modified by Qu et al. (2017). The merger trees are available at 28 snapshots between  $z = 20$  and  $z = 0$ , of which we use four in this paper:  $z = 0.27$ , 0.18, 0.1, and 0.

EAGLE has been found to reproduce many observed galaxy properties, including the  $z = 0$  Tully–Fisher relation (Schaye et al. 2015), the evolution of the galaxy stellar mass function (Furlong et al. 2015), the neutral gas masses of galaxies with  $10^{10} M_{\odot} < M_{*} < 10^{11} M_{\odot}$  (Bahé et al. 2016), the dependence

of galaxy HI content on environment (Marasco et al. 2016), the SFR– $M_{*}$  relation (Furlong et al. 2015), and the evolution of the star formation rate function (Katsianis et al. 2017). Galaxy and halo catalogs as well as particle data from EAGLE snapshots have been made publicly available (McAlpine et al. 2016).

## 2.2. Simulated Galaxy Sample Selection

We use the EAGLE merger trees to select a sample of galaxies that fall into clusters between  $z = 0.27$  and  $z = 0$ . Such galaxies should experience a wide range of ram pressures as they travel from outside the cluster to the pericenter of their orbits.

In EAGLE there are seven clusters (FoF groups) with  $M_{200c} > 10^{14} M_{\odot}$ <sup>6</sup> at  $z = 0$ . One of these consists of two merging clusters (individually more massive than  $10^{14} M_{\odot}$  at  $z = 0.1$ ) whose central galaxies are still separated by a distance of approximately  $5r_{200c}$ , and we thus treat the two components as separate clusters.

For each cluster at  $z = 0$ , we identify the FoF group containing the main progenitor of its central galaxy at each previous output, and treat this as the same cluster at a previous time. In practice, this is also the most massive FoF group that merges with others to become the  $z = 0$  cluster.

We choose to focus on galaxies that do not merge into clusters as satellites of larger structures, in which they may undergo so-called “preprocessing” (Fujita 2004). We defer analysis of a larger sample of galaxies in a broader range of environments to later work. We therefore select our galaxy sample according to the following criteria. We identify galaxies that at  $z = 0.1$ , 0.18, or 0.27 were not part of cluster FoF groups, and were the central galaxies of their own FoF group, but became members of a cluster FoF group in the subsequent snapshot. We note that the physical extent of FoF groups is typically larger than  $r_{200c}$ , and therefore a galaxy may join a cluster outside of this radius. We also searched for galaxies that were initially isolated and had merged with the central galaxy of the cluster by the next snapshot, indicating a rapid descent to the center of the cluster, but found no such objects.

We enforce cuts on the stellar and gas mass of our galaxy sample: they must initially have  $M_{*} > 10^9 M_{\odot}$  and  $M_{\text{gas}} > 10^9 M_{\odot}$ . Here the gas mass is the total mass of gas that is gravitationally bound to each galaxy subhalo, regardless of whether it is neutral or ionized; we will discuss the division of gas into different phases in Section 2.2.1.

As the purpose of this paper is to investigate ram pressure stripping, we select those galaxies that lose at least one-third of their initial gas mass by  $z = 0$ . Because we would like to focus on ram pressure stripping and exclude other evolutionary processes that significantly affect galaxies, we remove galaxies that the EAGLE merger trees indicate merge with an object larger than 5% of their stellar or gas mass between the initial redshift and  $z = 0$ . Also, we choose only those galaxies whose stellar mass does not decrease between the two snapshots during which they enter the cluster, aside from the mass lost due to the stellar mass loss prescription in EAGLE. This is to avoid selecting galaxies that are strongly affected by tidal interactions, which strip stars as well as gas. However, we do not exclude galaxies that lose stellar mass later in their

<sup>6</sup> Here  $M_{200c}$  is the mass within the virial radius  $r_{200c}$ , which is the radius within which the mean density is 200 times the critical density of the Universe, measured centered on the most bound dark matter particle within each FoF halo.



**Table 1**  
Simulated Galaxy Sample Properties

Infall Redshift	All Gas Removed	Gas Remains at $z = 0$	Merges with Cluster Central	Falsely <sup>a</sup> Merges with Cluster Central	Total
$0 < z < 0.1$	2	18	0	0	20
$0.1 < z < 0.18$	10	13	1	1	25
$0.18 < z < 0.27$	18	15	1	1	35

**Note.**

<sup>a</sup> SUBFIND may sometimes improperly identify two nearby galaxies as a single object. As a result, the particles of two galaxies in our sample are at one point assigned to the central cluster galaxy even though the galaxies reappear as separate objects in later outputs. Because we cannot track which particles are still bound to a galaxy in the outputs in which the particles are improperly assigned to the central object, we cease tracking the galaxy when this occurs.

evolution through the cluster, or simultaneously lose stellar mass and gain it via star formation. We analyze the potential influence of tides on our galaxy sample in the [Appendix](#), where we find that tidal interactions (with either other satellite galaxies or the cluster center) are unlikely to significantly influence the galaxies in our sample. We conclude that gas stripping in our galaxy sample is dominated by ram pressure.

We identify the selected galaxies in the short-timescale outputs (“snippets”) of the EAGLE simulation. We take the descendant of each galaxy to be the one that contains the majority of its star particles. For consistency in the sample, we eliminate galaxies that become satellites of larger groups at any point before cluster infall, as well as those that increase their baryonic (stellar plus gas) mass by over 5% at any point after the initial output, which we take to be the output at which the galaxy has its maximum baryonic mass.

We track these galaxies until one of three conditions is satisfied: the galaxy loses all of its gas mass, the galaxy merges with another galaxy (in practice, always the central galaxy of the cluster), or the end of the simulation ( $z = 0$ ) is reached. For the case of mergers, sometimes SUBFIND falsely “merges” two galaxies that are later identified as separate objects again. In this analysis, we cease tracking the galaxy when this occurs, but still retain it as part of our sample as long as its trajectory is at least five simulation outputs long and it loses at least 33% of its initial gas mass by that point. There are two galaxies in our final sample that falsely “merge” with the central galaxy in this manner and that we cease tracking at that time.

Selected in this manner, our final sample consists of 80 galaxies. Their infall redshifts and status at the time we stop tracking them are summarized in [Table 1](#).

### 2.2.1. Separation of Gas into Neutral and Ionized

We separate the gas bound to each galaxy into a neutral component and a hot ionized component. One reason to treat these separately is with consideration to observations: the two phases of gas are not observable in the same bands. The second reason that is more relevant to the current paper is that the neutral and ionized gas components have different geometries, with the former generally located in a flattened, rotating disk and the latter in a spheroidal halo. The two geometries are treated differently in common analytic models for ram pressure stripping, which will be described further in [Section 3.1](#).

EAGLE does not natively track different phases of gas. We instead employ the prescription used in [Bahé et al. \(2016\)](#) and [Crain et al. \(2017\)](#) to estimate the fraction of neutral (HI + H<sub>2</sub>) gas versus ionized hydrogen gas in each gas particle. The prescription is based on a fitting formula from [Rahmati et al. \(2013\)](#) with the temperature, pressure, and metallicity of each

gas particle as inputs, and an assumed value of the UV background from [Haardt & Madau \(2001\)](#). The fitting formula was derived from higher-resolution simulations of galaxies that implemented radiation transport modeling; details can be found in [Rahmati et al. \(2013\)](#). When applied to EAGLE galaxies, this prescription results in mean galaxy neutral gas masses within 0.1 dex of observations for galaxies with  $M_* > 10^{10} M_\odot$  at  $z = 0$  ([Bahé et al. 2016](#)), although galaxies with lower stellar masses are found to be HI deficient compared to observations ([Crain et al. 2017](#)).

Because we would like to trace the kinematics of individual gas particles, as we will describe in [Section 3.2](#), we do not divide the particles into neutral and ionized components, but rather simply label each gas particle as either “neutral” or “ionized” based on whether its neutral hydrogen fraction is above or below 50%. The distribution of the neutral hydrogen fraction of gas particles in EAGLE galaxies tends to be strongly bimodal ([Manuwal et al. 2022](#)), and thus the results should not depend significantly on the choice of 50% as the separation criterion. Neutral gas particles generally have temperature  $T \sim 10^4$  K, as EAGLE has an imposed temperature floor due to its finite resolution, while ionized gas has  $T \sim 10^5$ – $10^6$  K.

### 2.3. Galaxy Sample Properties

In [Figure 1](#), we present the initial properties of our sample, separated into “neutral” and “ionized” gas as described above. These are the properties of the galaxies in the first simulation output at which we begin tracking them, before they are significantly affected by ram pressure.

The left panel of [Figure 1](#) shows the initial mass of neutral and ionized gas in each galaxy, with the color representing the stellar mass. Our sample contains a variety of galaxies in stellar and gas mass. Galaxies with large  $M_*$  tend to possess very massive hot halos of ionized gas, whereas lower-mass galaxies have considerable variation in their neutral and ionized gas content.

The right panel of [Figure 1](#) shows the morphologies of the gas particle distribution separated into neutral and ionized gas, as well as that of the stellar component of each galaxy. Ellipticity is shown on the horizontal axis, such that more spherical objects are to the left of the plot, while triaxiality is shown on the vertical axis, such that oblate objects are to the lower right of the plot and prolate ones are to the top right. Despite the fact that the neutral gas component was not chosen based on morphology, most of the galaxies have neutral gas that lies in a flattened (oblate) disk. The stellar component of the majority of the galaxies is also flattened, with a minor-to-major axis ratio of  $< 0.5$ . The color of the points representing the stellar and neutral gas components indicates the relative

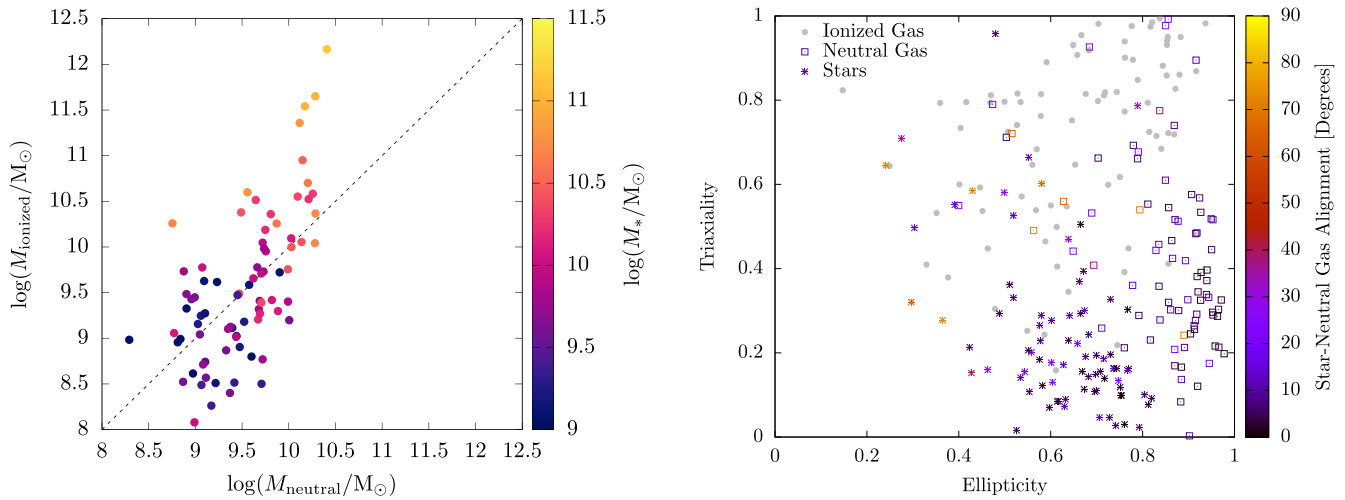


**Figure 1.** Initial properties of our selected ram pressure-affected galaxy sample. Left: neutral gas mass vs. ionized gas mass in each galaxy, where the masses are computed as the sum of the masses of the gas particles designated “neutral” or “ionized” based on their neutral hydrogen fraction (see Section 2.2.1). The color scale shows the stellar mass of each galaxy. Right: the initial morphology of the gas and stellar components of our galaxies, with square points representing the neutral gas, circular points representing the ionized gas, and star-shaped points representing the star particles. The horizontal axis represents the ellipticity  $\epsilon = 1 - c/a$ , while the vertical axis is the triaxiality  $T = (1 - b^2/a^2)/(1 - c^2/a^2)$ , where  $a \geq b \geq c$  are the axes computed from the reduced moment of inertia tensor of the particle distribution, similar to Thob et al. (2019). Objects to the left side of the plot are spherical whereas objects to the right side are flattened. Objects near the bottom right are oblate disks, whereas those near the top right are prolate. The color scale shows the angular difference between the minor axes of the stellar and neutral gas components of each galaxy, such that  $0^\circ$  indicates alignment.

alignment of the minor axes of the two. We see that in the majority of cases, the stars and neutral gas are aligned within  $20^\circ$ .

The majority of galaxies have a prolate distribution of the ionized gas particles bound to their subhalo. However, as we will see in Section 4.1, the density profile of the ionized gas can still be well approximated as spherical.

### 3. Ram Pressure Models

In this section, we first describe the analytic ram pressure models from the literature that will be used to predict the ram pressure stripping of the neutral gas disk and ionized halo, and will be compared to the stripping rate from the EAGLE simulation. We then describe a slightly more complex toy model that we will also compare to EAGLE in order to help explain the deviations of the analytic models from the simulation.

#### 3.1. Analytic Ram Pressure Models

The criterion for gas to be stripped from a galaxy by ram pressure was first described in Gunn et al. (1972). Gas can be stripped when the force of the ram pressure exceeds the restoring force exerted on the gas by the gravitational potential of the galaxy. This can be expressed as:

$$P_{\text{ram}} > \Sigma_{\text{gas}} g_{\text{max}}. \quad (1)$$

Here  $\Sigma_{\text{gas}}$  is the mass surface density of the galaxy gas integrated along the ram pressure direction, and  $g_{\text{max}}$  is the maximum restoring acceleration along the direction of the ram pressure.  $P_{\text{ram}}$  is the ram pressure, which is given by

$$P_{\text{ram}} = \rho_{\text{ICM}} v_{\text{rel}}^2, \quad (2)$$

where  $\rho_{\text{ICM}}$  is the density of the ICM through which the galaxy is passing, and  $v_{\text{rel}}$  is the relative velocity between the galaxy and the ICM.

We compute  $\rho_{\text{ICM}}$  and  $v_{\text{rel}}$  from the local ICM properties around each galaxy at each simulation output. The relevant ICM particles are taken to be those that pass through a sphere containing all of the gas bound to each galaxy, or through a sphere with 30 kpc radius if larger.<sup>7</sup> ICM particles with density above  $5 \times 10^{13} M_{\odot} \text{Mpc}^{-3}$  and temperature less than  $10^7$  K are excluded from consideration to avoid selecting cold, dense substructures within the cluster. The relative velocity is  $v_{\text{rel}} = v_{\text{ICM}} - v_{\text{CoM}}$ , where  $v_{\text{CoM}}$  is the center-of-mass velocity of the galaxy subhalo, and  $v_{\text{ICM}}$  is the ICM velocity.  $v_{\text{CoM}}$  is computed from the subhalo particles, but the ICM particles have a range of velocities. To obtain a single direction and magnitude for  $v_{\text{rel}}$ , we take its direction  $\hat{v}_{\text{rel}}$  to be the one that maximizes the value of  $\sum m_i \mathbf{v}_i \cdot \hat{v}_{\text{rel}} / \sum m_i$ , where  $m_i$  and  $\mathbf{v}_i$  are the masses and velocities of the ICM particles selected as described above. The summed quantity is taken to be the magnitude of the relative velocity. The median density of ICM particles with relative velocity direction within  $60^\circ$  of  $\hat{v}_{\text{rel}}$  is taken to be the value of  $\rho_{\text{ICM}}$ . The ICM velocity is assumed to be unidirectional and constant between simulation outputs. We find that our ram pressure magnitude estimates are generally similar to those computed using the prescription given in Marasco et al. (2016), even with small numbers of ICM particles passing through the galaxy.

The ram pressure computed in this manner is presented as the color scale in Figure 2, in which we show the trajectories of a subset of galaxies in our sample as they fall into their host clusters, as well as the evolution of their neutral and ionized gas masses. We see in the top row of panels that the ram pressure typically increases with decreasing distance to the center of the cluster, as expected. The second row of panels shows the evolution of the neutral gas mass of each galaxy, indicating that

<sup>7</sup> The median number of ICM gas particles used to compute the ram pressure is 1081, with an interquartile range 302–3456. Note that 3.8% of outputs have ram pressure estimates based on fewer than 50 particles; this is most commonly caused by very low ICM velocities relative to the galaxy, such that few ICM particles pass through the sphere containing the galaxy.

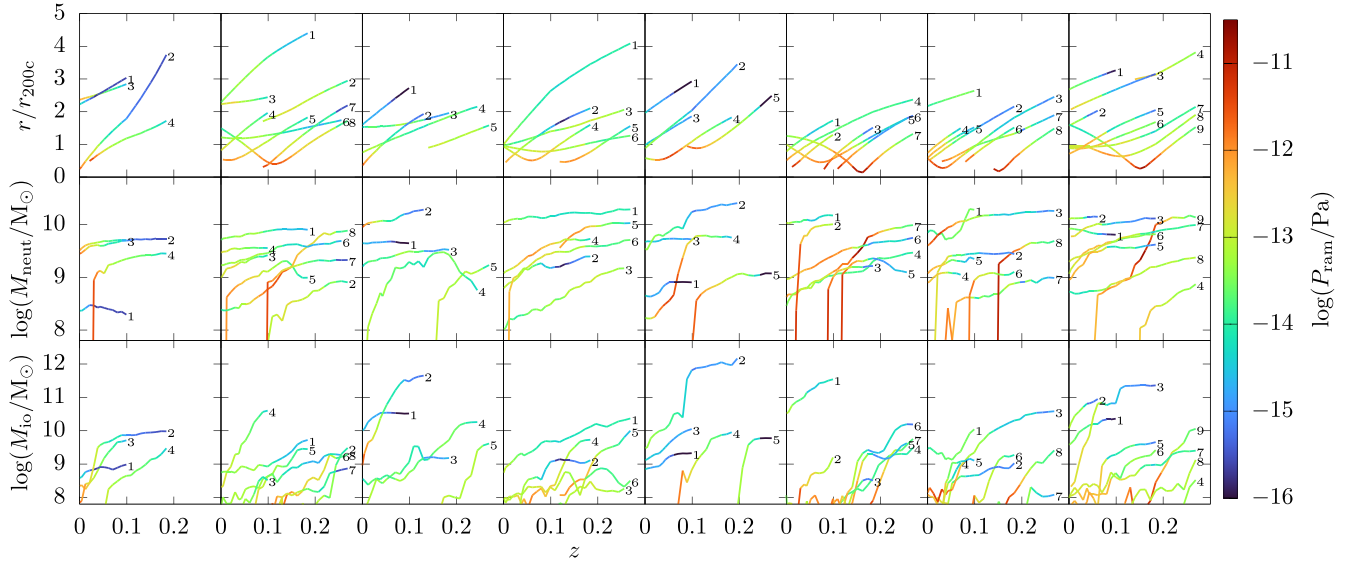


**Figure 2.** The evolution of a subset of the galaxies in our sample within the eight  $z=0$  EAGLE clusters ( $M_{200c} > 10^{14} M_{\odot}$ ). Each column represents one of the eight clusters, in order of increasing  $M_{200c}$  from left to right. The color scale in each panel shows the ram pressure computed from the local ICM as described in Section 3.1. For each cluster, galaxies are labeled with numbers to allow for identification between rows. Top row: the trajectory of each galaxy as a function of redshift, expressed as the 3D distance from the center of the cluster in terms of its  $r_{200c}$ . Middle row: the neutral gas mass of each galaxy as a function of redshift. Bottom row: the ionized gas mass of each galaxy as a function of redshift.

typically large ram pressures ( $P_{\text{ram}} \gtrsim 10^{-12.5}$  Pa) are required to efficiently strip neutral gas from the disk. Such conditions in most cases occur significantly within  $r_{200c}$ , during the galaxy’s pericenter passage. By contrast, the bottom row of panels shows that the ionized halo can be stripped by lower ram pressures, which occur even outside of  $r_{200c}$ .

For the right-hand term in Equation (1), we will adopt different analytic approximations for the neutral gas disk and the quasi-spherical ionized gas halo: the former from Gunn et al. (1972), and the latter from McCarthy et al. (2008).

In Gunn et al. (1972), an analytic approximation for Equation (1) is given for the case of a perfectly flat stellar and gas disk whose motion relative to the ICM is perpendicular to the disk direction (face-on):

$$g_{\text{max}} = 2\pi G \Sigma_{*}, \quad (3)$$

where  $\Sigma_{*}$  is the stellar disk mass surface density. Thus, the analytic stripping criterion for the neutral gas disk would be:

$$P_{\text{ram}} > 2\pi G \Sigma_{*} \Sigma_{\text{gas}}. \quad (4)$$

We implement this model by computing the stellar and gas surface mass densities in the direction perpendicular to the plane of the stellar disk (which, as shown in Figure 1, is typically well aligned with the neutral gas disk). We obtain these surface densities by smoothing the particles with a 2D Wendland C2 kernel (Wendland 1995) with 58 neighbors.<sup>8</sup> Since the gas density in the simulation is based on smoothing over all gas particles regardless of their subgroup membership, for the gas mass surface density we also smooth over the nearest 20 kpc of ICM particles. To verify that the results are robust to this choice, we also computed them using the gas surface density from only the gas particles in the galaxy. By construction, this underpredicts the simulation gas surface density; however, while the resulting stripping timescales are shorter, our results remain qualitatively similar.

<sup>8</sup> This kernel is akin to that used for SPH smoothing in EAGLE, but 2D rather than 3D.

For each simulation output, we compare the value of  $P_{\text{ram}}$ , computed as described above, to the value of  $\Sigma_{\text{gas}} g_{\text{max}}$  for each gas particle. Once  $P_{\text{ram}}$  exceeds  $\Sigma_{\text{gas}} g_{\text{max}}$ , we consider the particle to have been stripped in the analytic model.

An analytic approximation for a spherical halo, such as that in which the hot ionized gas typically resides, is given in McCarthy et al. (2008). Assuming isothermal gas and dark matter halo profiles, they find:

$$g_{\text{max}} = \frac{GM(<r)}{2r^2} \text{ and } \Sigma_{\text{gas}} = \pi r \rho_{\text{gas}}(r), \quad (5)$$

where  $M(<r)$  is the total mass of the subhalo within radius  $r$ , and  $\rho_{\text{gas}}(r)$  is the gas density at  $r$ . This gives the stripping criterion as:

$$P_{\text{ram}} > \frac{\pi}{2} \frac{GM(<r)\rho(r)}{r}. \quad (6)$$

However, for more general power-law profile models for the gas and dark matter halos, the resulting equation is:

$$P_{\text{ram}} > \alpha \frac{GM(<r)\rho(r)}{r}, \quad (7)$$

where  $\alpha$  depends on the choice of profiles. McCarthy et al. (2008) found  $\alpha=2$  to be the best fit to the results of their hydrodynamical simulations.

In our implementation of this model, we use a power-law fit to the density of the ionized gas particles for  $\rho(r)$ . We note that the density of each particle in EAGLE is computed using kernel smoothing over *all* nearby gas particles, including those not part of the ionized halo.

We also attempted to use a power law for the total subhalo mass profile  $M(<r)$ , but found that it was poorly fit by any single power law, instead typically being well described by an NFW profile (Navarro et al. 1996). We thus use the true subhalo mass profile measured around the most bound particle when computing Equation (7), which includes the mass from all particle types (dark matter, stars, and gas).

Additionally, we tried using the radially smoothed density of the ionized gas for  $\rho(r)$  rather than a power-law fit. This produced qualitatively similar results to those presented in Section 4.3.

### 3.2. Ram Pressure Toy Model

The analytic models described in the previous subsection rely on a number of idealized assumptions, specifically regarding the geometry of the galactic gas and gravitational potential well, as well as the orientation of the galaxy relative to the ram pressure direction. In this subsection, we describe a toy model that treats these in a more realistic fashion while nevertheless being more simplified than a full hydrodynamical simulation. We use this model to investigate whether adding to the complexity of analytic models can improve their agreement with hydrodynamical simulations. Additionally, we use it to systematically analyze the physical reasons why the analytic model differs from the simulation.

The toy model is more complex than the analytic models in that the gravitational potential distribution of the subhalo and the orientation of the galaxy relative to the ram pressure direction are taken from the simulation, and the orbits of gas particles are integrated rather than the direction of stripping being assumed to be vertical from the initial position. The inclination of a galaxy relative to the ram pressure is known to make a difference to the stripping rate (Roediger & Brüggén 2007), and can cause changes to the gas morphology, such as unwinding the spiral arms of galaxies that are being stripped edge-on (Bellhouse et al. 2021).

The toy model is still simplified relative to hydrodynamical simulations in a number of respects. The gas particles are treated as test particles within the subhalo gravitational potential, and hydrodynamical interactions between the gas particles are neglected, as are all subgrid physics effects. Because the dark matter is the largest contributor to the gravitational potential of the subhalo and is unaffected by ram pressure, we find that the evolution of the subhalo potential due to change in the distribution of gas between outputs spaced by  $\approx 120$  Myr is generally small. However, as we will describe in Section 5, hydrodynamical effects and subgrid physics have significant influence on the ram pressure stripping process in EAGLE.

The toy model also distributes the force of the ram pressure over the galactic gas in a simplified fashion. As described in Section 3.1, the ram pressure is computed from the local ICM properties as  $P_{\text{ram}} = \rho_{\text{ICM}} v_{\text{rel}}^2$ . Unlike for the analytic models, in the toy model  $v_{\text{rel}} = v_{\text{ICM}} - v_{\text{gas}}$ , where  $v_{\text{gas}}$  is the velocity of each individual gas particle in the galaxy. The acceleration of each gas particle is then estimated as  $a_{\text{ram}} = P_{\text{ram}} / \Sigma_{\text{gas}}$ , where  $\Sigma_{\text{gas}}$  is the gas surface density integrated along the ram pressure velocity direction, computed as described in Section 3.1. This formulation for the acceleration due to ram pressure is oversimplified, as it does not take into account the fact that gas at the front of the galaxy “shields” the gas behind it from ram pressure (Jáchym et al. 2009). Using a value of  $\rho_{\text{ICM}} v_{\text{rel}}^2$  for the ram pressure magnitude also relies on the assumption that the ICM wind deposits its full momentum into the gas of the oncoming galaxy. As we will discuss in Section 5.2, this assumption is inaccurate.

We recompute  $\Sigma_{\text{gas}}$  as we evolve the motions of the gas particles in the toy model, and estimate the acceleration due to ram pressure using the instantaneous value of  $\Sigma_{\text{gas}}$ . By contrast, we update the gravitational potential of the subhalo to that in the simulation only at the beginning of each integration, and

also change the ram pressure magnitude and direction based on the local ICM properties only at this time.

The gravitational potential within each subhalo is interpolated from the outputs of SUBFIND. This interpolation does not extend outside the boundaries of the subhalo identified by SUBFIND, which uses saddle points in the density distribution to define the physical extent of subhalos. When particles exit this region, we assign them a potential of 0, such that they are always unbound.

We make two different types of comparisons using the toy integration. For the first, we select all of the gas particles bound to the galaxy in the initial simulation output at which we identify it (before it enters the cluster FoF group), and integrate the motion of these particles under the assumptions above for the entire time that we track the galaxy in the simulation. That is, we use the positions and velocities that we obtain for the gas particles at the end of each integration to be the initial conditions for the next integration, but we update the subhalo potential and ram pressure magnitude and direction to be those computed for the new simulation output. We ignore any new gas particles that are accreted to the galaxy since the time at which we begin tracking it, although as described in Section 2.2, we have selected galaxies that accrete very little gas. We will use these results to compare the stripped mass fraction predicted by the analytic models, toy model, and simulation, and to identify the main reasons why the analytic models differ from the simulation.

For the second comparison, we will perform the toy model integration separately between individual simulation outputs. We will then compare each toy model result to the subsequent output. This approach should result in less divergence from the simulation results, as the toy model integration is run for only a short time. We will perform the second comparison only between the toy model and the simulation, in order to present subgrid and hydrodynamical effects that have a significant impact on the outcome of ram pressure stripping.

We are interested in comparing the fraction of gas mass stripped in the toy model, analytic models, and simulation. However, this depends on the definition used for stripped gas. In the analytic models described in Section 3.1, gas is assumed to be stripped when the force of the ram pressure exceeds the gravitational restoring force on the gas. As discussed in, for example, Köppen et al. (2018), this is not identical to the gravitational unbinding of the gas, which is when the gas velocity exceeds the escape speed of the subhalo. Gas for which the maximum restoring force has been exceeded is generally not yet energetically unbound. Additionally, gas that experiences a rapid impulse of ram pressure can achieve escape velocity and become energetically unbound despite the ram pressure not exceeding the maximum gravitational restoring force.

EAGLE does not output any data related to the acceleration experienced by particles, and thus we do not have a record of whether every gas particle exceeded its maximum restoring force to compare directly to the analytic models. For the simulation, we compute the sum of the kinetic and potential energy of each gas particle and designate the particle as unbound if this value is larger than zero.<sup>9</sup> Particles that exit the

<sup>9</sup> In EAGLE, thermal energy also contributes to whether a gas particle is considered energetically unbound or not, but here we are only interested in a kinematic comparison, and we thus ignore this term. For neutral gas, which is cold, the median ratio of the thermal energy to the sum of the kinetic and potential energies is less than 1%. For the hotter ionized gas, the median contribution is 21% for particles in galaxies at low ram pressures ( $< 10^{-15}$  Pa) and decreases to 4% for particles in galaxies at high ram pressures ( $> 10^{-12}$  Pa).



**Table 2**  
Summary of Computed Quantities for  $i$ th Gas Particle at Each Simulation Output Time

		$\Sigma_{\text{gas},i}$	$g_{\text{max},i}$	$\Phi_i$	$\mathbf{r}_i, \mathbf{v}_i$
Analytic	Disk	$\int \rho_{\text{gas}}(r)$ along disk minor axis at initial time	$GM(<r_i)/r_i^2$ at initial time	...	...
	Halo	$2r_i\rho_{\text{gas}}(r_i)$ with $\rho_{\text{gas}} \propto r_i^{-3}$ at initial time	...	...	...
Toy Model (Cumulative)		$\int \rho_{\text{gas}}(r)$ along $\hat{v}_{\text{rel}}$ direction at each time, starting with <i>predicted</i> gas positions	$\max(-\mathbf{g}(\mathbf{r}) \cdot \hat{v}_{\text{rel}})$ during each vertical orbit; $g = -\nabla\Phi$ ; $\mathbf{r}_i$ from cumulative prediction	$\Phi(\mathbf{r}_i); \Phi(\mathbf{r})$ from each simulation output, $\mathbf{r}_i$ from <i>cumulative</i> prediction	<i>cumulative</i> prediction
Toy Model (Single-Step)		$\int \rho_{\text{gas}}(r)$ along $\hat{v}_{\text{rel}}$ direction at each time, starting with <i>simulation</i> gas positions	...	$\Phi(\mathbf{r}_i); \Phi(\mathbf{r})$ from each simulation output, $\mathbf{r}_i$ from <i>single-step</i> prediction	<i>single-step</i> prediction
EAGLE Simulation		...	...	direct output from simulation	direct output from simulation

**Note.** The quantities obtained from the models described in Sections 4.3 and 5, as well as the EAGLE simulation, at each simulation output time. The relevant quantities for each gas particle are: the local gas surface density  $\Sigma_{\text{gas}}$ , the maximum gravitational restoring acceleration experienced by the particle  $g_{\text{max}}$ , the gravitational potential energy per unit mass  $\Phi$ , the position  $\mathbf{r}$ , and the velocity  $\mathbf{v}$ . Other quantities mentioned in the table above include  $\rho_{\text{gas}}$ , the 3D density of the gas, and  $\hat{v}_{\text{rel}}$ , the unit vector in the direction of the relative velocity between the ICM and the galaxy (i.e., the direction of the ram pressure force). The criterion for ram pressure stripping from Gunn et al. (1972) is  $P_{\text{ram}} > \Sigma_{\text{gas}}g_{\text{max}}$ . The criterion for a particle being unbound (exceeding the escape speed) is  $E/m = \Phi + v^2/2 \geq 0$ . The results of the analytic model, cumulative toy model, and simulation are compared in Section 4.3. The results of the single-step toy model and simulation are compared in Section 5.

region of the SUBFIND subhalo defined by saddle points in the density are no longer assigned to that subhalo, and are assigned a potential energy of 0.

In the toy model, we compute both the energy of each gas particle and whether it exceeded the maximum restoring force it encountered within its last vertical oscillation, and compare these to the simulation and analytic models, respectively.

In Section 4.1 we will examine the analytic model assumptions for the initial conditions of the subhalo potential and gas distribution, and determine the model parameters that best agree with the simulation, which we will then use throughout the rest of Section 4. A summary of the different models described in this Section—analytic, toy, and simulation—can be seen in Table 2, which presents the outputs of the models for each gas particle and how they are obtained. This table presumes the analytic model parameters from Section 4.1, which will be explained immediately below.

#### 4. Comparison of Model Results

Here we compare the predictions of the analytic and toy models described in Section 3, and those of the EAGLE reference simulation described in Section 2.1.

##### 4.1. Evaluation of Analytic Model Initial Assumptions

As described in Section 3.1, we employ two analytic models from the literature to predict the total (cumulative) gas mass stripped from the neutral gas disk and ionized hot gas halo of galaxies. These models make assumptions about the geometry of these gaseous components, as well as about the gravitational potential in which the gas resides.

In Figure 3, we present the ratio of the initial parameters assumed in the analytic models to the initial parameters from the simulation/toy model, as a function of the initial stellar mass of each galaxy. The left panels show the comparison for the ionized gas, which in the analytic models is assumed to be spherically distributed and also reside in a subhalo with spherically symmetric mass distribution. The right panels show

the comparison for the neutral gas, which is assumed to be in a flat disk perpendicular to the direction of the ram pressure, with the restoring force produced by a stellar disk in the same plane. This is described in detail in Section 3.1.

The top panels of Figure 3 show the log of the ratio of  $\Sigma_{\text{gas}}g_{\text{max}}$  assumed in the analytic model, to that in the toy model at the initial time. Specifically,  $\Sigma_{\text{gas}}$  is the gas mass surface density at the location of each gas particle, while  $g_{\text{max}}$  is the maximum gravitational restoring acceleration opposing the ram pressure that is encountered by each gas particle. The center and bottom panels of Figure 3 directly compare  $g_{\text{max}}$  and  $\Sigma_{\text{gas}}$  from the analytic models to their values from the simulation/toy model.

For the toy model,  $\Sigma_{\text{gas}}$  is measured directly from the gas distribution in the simulation, integrated in the direction of the ram pressure in the initial simulation output.  $g_{\text{max}}$  is the maximum restoring acceleration in the first vertical orbit of each gas particle (which can be multiple outputs long); this value is not reported by the EAGLE simulation and is thus taken from the toy model integration. The analytic models for  $\Sigma_{\text{gas}}$  and  $g_{\text{max}}$  of the neutral gas disk and ionized gas halo are presented in Section 3.1.

For the ionized halo analytic model,  $\Sigma_{\text{gas}}g_{\text{max}}$  has the form described in Equation (7). The top-left panel of Figure 3 shows the distribution, in terms of median and quartiles, of the log of the ratio of  $\Sigma_{\text{gas}}g_{\text{max}}$  for the ionized gas particles in each of the 80 galaxies in our sample. If the toy model and analytic model were always in agreement, the value would be zero. If  $\alpha$  in Equation (7) is taken to be  $\pi/2$ , as it would be if both the gas and total matter distribution of the subhalo had an isothermal density profile,  $\log(\Sigma_{\text{gas}}g_{\text{max}})$  for the analytic model differs from that for the simulation/toy model by  $-0.32 \pm 0.04$  dex (blue points). Alternatively, the red points show  $\alpha = 2$ , which McCarthy et al. (2008) found was in better agreement with their hydrodynamical simulations, and which we find to perform slightly better than  $\alpha = \pi/2$ , being on average different from the toy model by  $-0.20 \pm 0.05$  dex.



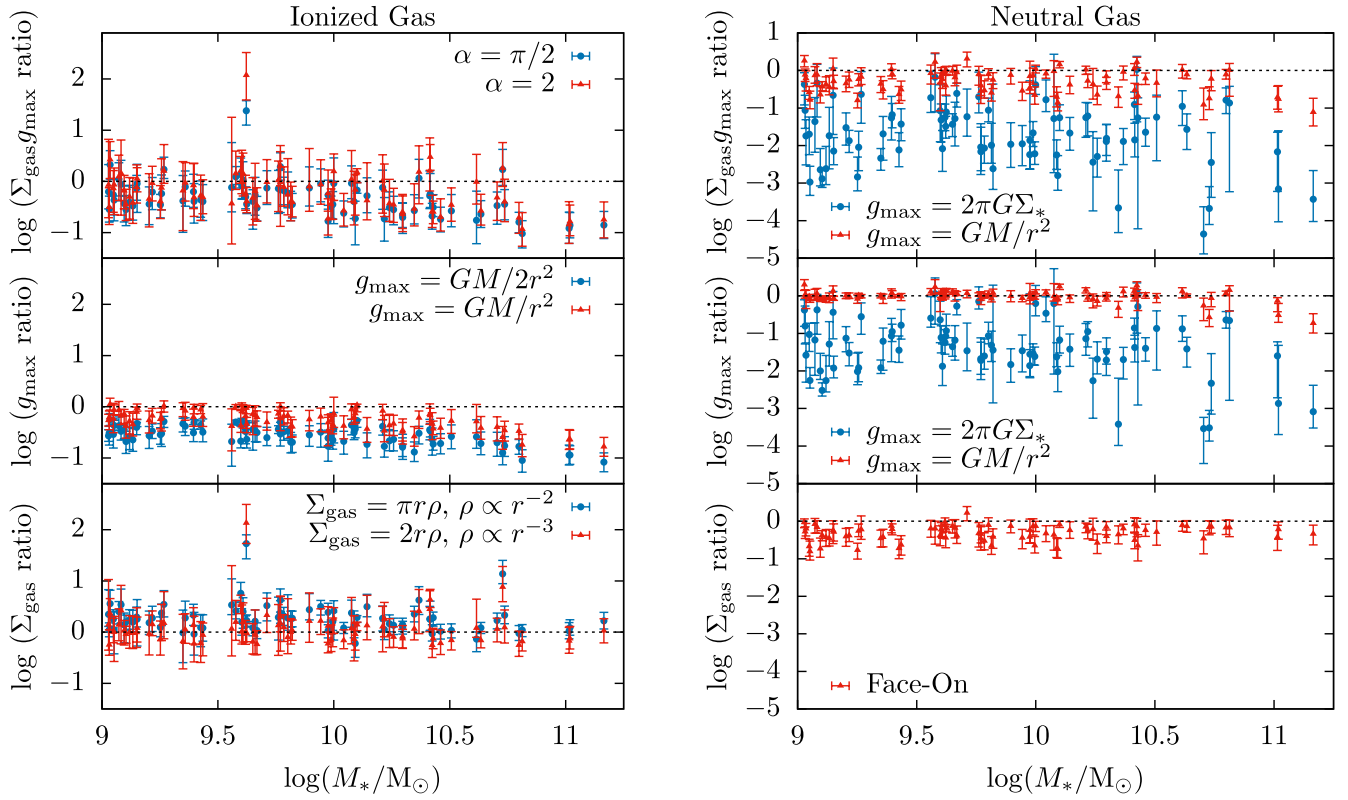


**Figure 3.** Ratio between galaxy parameters assumed by the analytic models (Section 3.1) and the initial parameters from the simulation/toy model (see Section 4.1 for explanation), as a function of initial galaxy stellar mass. Parameters for the ionized gas halo are presented on the left and those for the neutral gas disk on the right. From bottom to top, the parameters shown are gas surface density  $\Sigma_{\text{gas}}$ , maximum gravitational restoring acceleration  $g_{\text{max}}$ , and  $\Sigma_{\text{gas}}g_{\text{max}}$ , which must be exceeded by the ram pressure to strip the gas particle. Each of the 80 galaxies in our sample is represented by a point with error bars, indicating the median and quartile values of the ratio of analytic to simulation/toy parameters for all of the gas particles initially bound to the galaxy. Different point colors show different assumptions for the analytic models presented in Section 3.1, as explained in Section 4.1.

Greater disagreement can be seen when comparing  $\Sigma_{\text{gas}}$  and  $g_{\text{max}}$  individually between the analytic and toy models. This is presented for the ionized gas in the center-left and bottom-left panels of Figure 3. In the center-left panel, we see as the blue points  $g_{\text{max}} = GM/2r^2$ , which is the form for an isothermal dark matter halo. Note, however, that we have used the actual subhalo mass profile from the simulation for  $M(< r)$ , as described in Section 3.1, since the mass profile is described by an NFW form rather than any single power law. Here we see that this form gives a value for  $g_{\text{max}}$  on average  $-0.56 \pm 0.02$  dex away from the toy model value. The maximum possible finite value for  $g_{\text{max}}$  from a power-law model is  $g_{\text{max}} = GM/r^2$ , corresponding to  $M \propto r^2$ . This is plotted as the red points, again taking the simulation mass profile for  $M(< r)$  rather than a power law. We see that it is a better fit to the toy model value of  $g_{\text{max}}$ , but still differs on average by  $-0.26 \pm 0.02$  dex, despite giving the highest possible values for a power-law coefficient. This is likely because, as we note, the subhalo mass profile is not well fit by a single power law.

The ratios in Figure 3 are plotted as a function of the initial stellar masses of the galaxies. We see that for  $g_{\text{max}}$  of the ionized gas, the discrepancy between the analytic model and the toy model increases with increasing galaxy mass. Galaxies with the highest stellar masses initially possess very massive ionized halos of gas (see Figure 1) that cause the total subhalo mass profile to deviate from an NFW. All other properties in Figure 3 have little correlation with the galaxy stellar mass.

The bottom-left panel of Figure 3 compares  $\Sigma_{\text{gas}}$  between the analytic and toy models for the ionized halo, with blue points

showing the results for an  $r^{-2}$  (isothermal) fit to the ionized gas density profile, and the red points showing the results for an  $r^{-3}$  fit. We see that the latter fit is better: the mean deviation from  $\Sigma_{\text{gas}}$  in the simulation is only  $0.07 \pm 0.03$  dex, whereas for the isothermal fit it is  $0.26 \pm 0.03$  dex. We note that  $r^{-3}$  would correspond to the density profile of the ionized halo following that of the dark matter for the outer part of an NFW profile.

While  $g_{\text{max}}$  and  $\Sigma_{\text{gas}}$  are not individually well fit by the assumption of isothermal profiles for both the subhalo and gas mass profiles, it is notable that in combination they nevertheless produce reasonable values for  $\Sigma_{\text{gas}}g_{\text{max}}$  for the ionized halo. Nevertheless, we will take  $g_{\text{max}} = GM/r^2$  and  $\rho_{\text{gas}} \propto r^{-3}$  when comparing the analytic model to the toy model and simulation in Section 4.3, as these parameters produce slightly better results and are in agreement with the findings of McCarthy et al. (2008) regarding the value of  $\alpha$ .

The right panels of Figure 3 similarly compare the analytic model to the initial conditions of the toy model, but for the neutral gas disk, the analytic model for which is given by Equation (4). The blue points in the top panels show the ratio of  $\Sigma_{\text{gas}}g_{\text{max}}$ , where we see that the formulation from Gunn et al. (1972) differs from the expected value from the toy model by an average of  $-1.70 \pm 0.09$  dex—i.e., the ram pressure required to strip the gas is underestimated by a factor of  $\sim 50$ . We also show the ratio using  $g_{\text{max}} = GM/r^2$ , the maximum restoring acceleration we have chosen for the ionized gas, as red points. Since the neutral gas disk and ionized gas halo reside in the same potential, they should experience the same maximum restoring acceleration, and this

approximation to  $\Sigma_{\text{gas}} g_{\text{max}}$  is more similar to the simulation/toy model, differing by only  $-0.34 \pm 0.03$  dex.

The right-center panels again show the ratio of  $g_{\text{max}}$  for the analytic model to that from the toy model, now for the neutral disk. This underscores the fact that Equation (3) underestimates the gravitational force experienced by the gas particles: the value of  $g_{\text{max}}$  differs from that of the toy model by an average of  $1.36 \pm 0.08$  dex (blue points). By contrast, assuming  $g_{\text{max}} = GM/r^2$ , where  $M$  is the measured mass profile of the subhalo, the deviation from  $g_{\text{max}}$  in the toy model is a negligible  $-0.01 \pm 0.02$  dex (red points). This agreement is even better than for the ionized halo, likely because the neutral gas disk lies at the center of the subhalo where the NFW profile is similar to a power law with  $M \propto r^2$ . We conclude that taking into account the mass contribution from dark matter rather than only stars strongly affects the predicted ram pressure stripping of the neutral gas disk, and adopt  $g_{\text{max}} = GM/r^2$  for the neutral disk for the remainder of Section 4.

Finally, in the bottom-right panel, we see the ratio of  $\Sigma_{\text{gas}}$  for the neutral gas disk in the face-on direction to that using the true initial ram pressure direction. As expected, assuming that the galaxy is falling face-on into the ICM minimizes the value of  $\Sigma_{\text{gas}}$ . However, the difference is less than one magnitude, which is smaller than that from not taking into account the effect of dark matter on the gravitational restoring force.

We conclude from Figure 3 that it seems possible to achieve a good fit to the initial conditions for both the ionized gas halo and neutral gas disk using relatively simple analytic models for the gas surface density and maximum restoring acceleration. Nevertheless, we see across all of the panels that there is variation in the level of agreement between the analytic and toy models within the galaxy sample, presumably due to the differing gas and dark matter geometries in real galaxies relative to an idealized approximation.

For the remainder of this section, when comparing the analytic formulations to the toy model and simulation, we use the better-fitting analytic models in Figure 3. That is, we use  $\alpha=2$  for the ionized halo analytic model (defined in Equation (7)) and  $g_{\text{max}} = GM/r^2$  for the neutral gas disk (rather than Equation (3)) in the following comparisons. These choices, as well as those made for the toy model, are summarized in Table 2.

#### 4.2. Evolution of the Surface Density and Maximum Restoring Acceleration

We have just seen that the analytic models described in Section 4.1 are capable of reproducing the initial values of the gas mass surface density  $\Sigma_{\text{gas}}$  (from the simulation) and the maximum gravitational restoring acceleration  $g_{\text{max}}$  (inferred from the toy model) within  $\sim 0.3$  dex, given the correct choice of parameters. These analytic models make the simplifying assumption that the direction of the ram pressure is constant throughout the stripping process, and that the gas particles do not change their distribution in the perpendicular plane over that time. As a result,  $\Sigma_{\text{gas}}$  and  $g_{\text{max}}$  are assumed to be constant values in these models.

However, both the effective  $\Sigma_{\text{gas}}$  and  $g_{\text{max}}$  can evolve as a real galaxy is stripped by ram pressure. Köppen et al. (2018) noted that  $g_{\text{max}}$  can change because the force of ram pressure can alter the orbits of gas particles. Additionally, the gravitational potential experienced by the gas changes over time as the gas is stripped. The gas surface density can also

change due to the fact that the ram pressure changes direction over the orbit of the galaxy in the cluster, causing the gas distribution perpendicular to the ram pressure direction to vary. Because the toy model evolves the orbits of the particles under the ram pressure force, and also updates the ram pressure direction and gravitational potential of the subhalo at each simulation output, it should account for all of these effects, albeit imperfectly.

In Figure 4, we show the range of evolution of  $\Sigma_{\text{gas}}$  and  $g_{\text{max}}$  predicted by the toy model. At each simulation output, we take the gas particles in each galaxy that the toy model predicts are still gravitationally bound, and compute for each particle the value of  $\Sigma_{\text{gas}}$ , the local gas mass surface density at the particle's location perpendicular to the direction of the ram pressure in that output, and  $g_{\text{max}}$ , the maximum gravitational acceleration in the direction opposing the ram pressure during the vertical orbit that the particle is undergoing. We then take the ratio of these values to the initial values of  $g_{\text{max}}$  and  $\Sigma_{\text{gas}}$  for those particles. We compute the median of these values for each galaxy and then display the interquartile range of these median values as a function of time in Figure 4. The top and bottom panels show the results for the ionized and neutral gas, respectively. From the light-blue regions in Figure 4, we see that  $g_{\text{max}}$  tends to increase slightly for the gas particles in the galaxies in our sample, but typically by less than 0.1 dex. This implies that evolution in  $g_{\text{max}}$  experienced by gas particles, due to either changes in their orbits or the evolution of the subhalo gravitational potential, is a minor factor in determining the ram pressure stripping rate.

The situation is different for the evolution of  $\Sigma_{\text{gas}}$ , shown as the orange regions. Here we see that for the neutral gas disk, the gas mass surface density seen by the ram pressure tends to decrease over time, by a median value of  $\sim 0.4$  dex over 2 Gyr. By contrast,  $\Sigma_{\text{gas}}$  of the ionized gas in most galaxies increases slightly, by a median value of  $\sim 0.1$  dex. There also appears to be a substantial range in the evolution of the gas surface density of different galaxies for both the neutral and ionized gas. We would expect galaxies with decreasing  $\Sigma_{\text{gas}}$  to undergo faster gas removal and those with increasing  $\Sigma_{\text{gas}}$  to be stripped more slowly.

However, we also show in Figure 4 the evolution of  $\Sigma_{\text{gas}}$  from the distribution of gas measured directly from the simulation rather than that predicted by the toy model. This is represented by the red dashed lines. Here we use the particles that are gravitationally bound in the simulation at each time, rather than those predicted to be bound by the toy model, but we find that this is not the main cause of the differences between the toy model and simulation. We see that  $\Sigma_{\text{gas}}$  is higher for both the neutral and ionized gas in the simulation than in the toy model, with the difference between the two increasing with time. We will argue in Section 5 that this is the result of two hydrodynamical effects that are present in the EAGLE simulation but not accounted for in the simple toy model: cooling of the ionized gas, and an inward force caused by deflection of the ICM flow.

Because the next subsection (Section 4.3) involves comparing the stripping timescales from the toy model to those from the analytic models described in Section 3.1, we will use the evolution of  $\Sigma_{\text{gas}}$  from the toy model to color-code the figures there. However, we note that if we instead use  $\Sigma_{\text{gas}}$  from the simulation, the qualitative trends that we see are similar, implying that some of the evolution in the simulation is via the

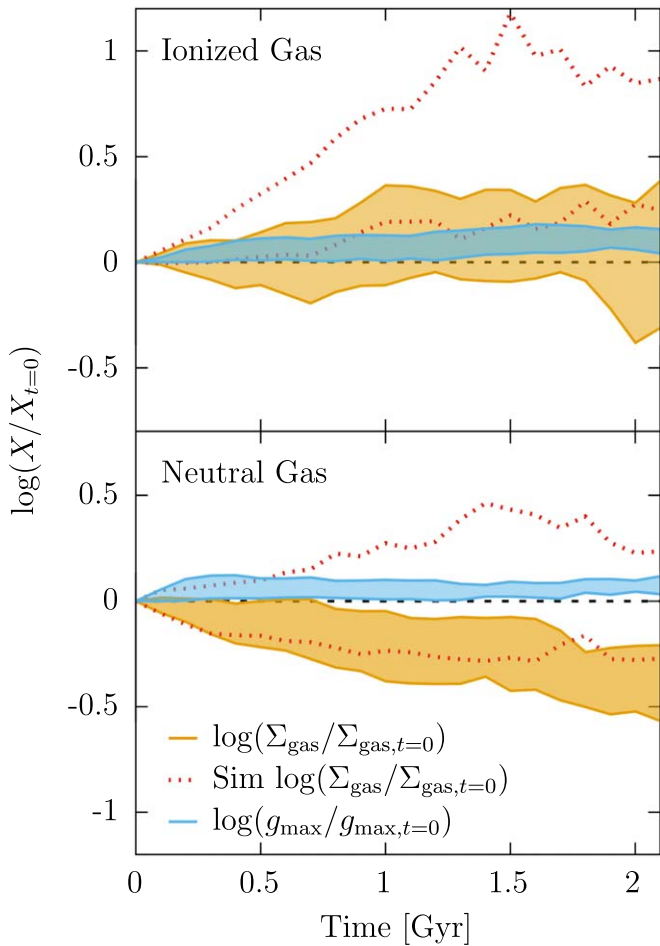


**Figure 4.** The evolution of the gas surface density  $\Sigma_{\text{gas}}$  and the maximum gravitational restoring acceleration  $g_{\text{max}}$  for the gas particles in our sample of 80 galaxies. The top panel shows the evolution of these values for the ionized gas, and the bottom panel for the neutral gas. At each time, we compute the ratio of  $\Sigma_{\text{gas}}$  and  $g_{\text{max}}$  to their initial values for each of the ionized or neutral gas particles that are still bound to each galaxy, and then take the median value for each galaxy. We then show the quartiles encompassing these median values as the shaded region in each panel. The light-blue region represents the range of the evolution of  $g_{\text{max}}$  in the toy model. The orange region is the evolution of  $\Sigma_{\text{gas}}$  in the toy model. The red dashed lines represent the evolution of  $\Sigma_{\text{gas}}$  in the simulation, computed by taking the true (rather than predicted from the toy model)  $\Sigma_{\text{gas}}$  in the direction of the ram pressure at each time, for the particles that are still bound in the simulation (rather than the toy model).

same processes in the toy model, despite the additional influence of hydrodynamics.

### 4.3. Cumulative Ram Pressure Stripping Predictions

We now compare different measures of cumulative stripping from the analytic model, toy model integration, and simulation results to determine how much simple analytic models differ from simulation results and the causes of that difference.

Figures 5 and 6 present stripping timescales from different models for the ionized and neutral gas, respectively. We note that these timescales are measured from the initial time at which we begin tracking the galaxy, and thus depend on the distance from the cluster center at which the galaxy enters the cluster FoF group, as well as the trajectory of the galaxy through the cluster and the cluster properties (see Figure 2). The timescales are linearly interpolated from the stripped fraction at each model/simulation output.

Because our toy and analytic models do not include star formation, gas particles that become stars by the next simulation output are fully excluded from the gas particle population when computing the stripped fractions of gas for all of the models. Similar results are obtained if excluding at each time all of the gas that will become stars by the final simulation output at which the galaxy is considered. For the gas that is initially ionized, typically little of it becomes stars by the time that we cease tracking the galaxy: the range is 0.02%–17%, with median value 4%. However, for most galaxies a substantial fraction of the initial neutral gas is converted to stars by the time that we cease tracking them: the range is 1%–58%, with median 28%. We note that these values are the original mass in gas that is converted to stars; star particles in EAGLE lose mass over time that is added to nearby gas particles, based on a prescription for stellar mass loss. In the figures presented in this section, we express all stripped mass fractions as a function of the initial mass of the gas particles.

Panels (a)–(d) of Figure 5 present the timescale at which 25% of the ionized gas is stripped from each galaxy. In panel (a), the horizontal axis is the timescale at which 25% of the gas is energetically unbound in the simulation, while the vertical axis is the same timescale for the ram pressure force to exceed the maximum restoring force ( $P_{\text{ram}} > \Sigma_{\text{gas}} g_{\text{max}}$ ) in the analytic model. We see that the analytic model typically substantially underestimates the 25% stripping time. The numbers in the bottom right of the panel give the median deviation (plain text) and median absolute deviation (italics) of the vertical axis value from the horizontal axis value, in megayears. Because some values in each panel are lower limits (arrows) where one of the models did not reach the given stripped fraction, the mean deviation is not always defined, and therefore sometimes a range of values is given for the median. This median also excludes those galaxies for which both models being compared give lower limits for the stripping timescale (i.e., for which neither model reached the stripped fraction in question). The median deviation values in panel (a) show that the analytic model typically estimates a 25% stripping timescale for the ionized gas that is 300 Myr shorter than the timescale from the simulation, and the median absolute deviation between the timescales is the same (314 Myr).

Panels (b)–(d) use the toy model to elucidate the origin of the difference between the analytic model and simulation. Panel (d) again shows the timescale from the simulation, now versus the 25% unbinding timescale from the toy model. Here we see that that the toy model accurately predicts the timescale at which 25% of the ionized gas is gravitationally unbound from the subhalo: the median deviation from the simulation is only  $\approx 55$  Myr, with a median absolute deviation (scatter) of  $\approx 162$  Myr. Therefore, it seems that hydrodynamical and subgrid effects are not the main reason for the difference between the simulation and the analytic model at this timescale, as they would also be present between the simulation and toy model.

Instead, we see in panel (c) that in the toy model, the timescale for the ram pressure force to exceed the maximum restoring force is shorter than the timescale for the gas to become gravitationally unbound, by a median value of  $\approx 159$  Gyr. This is as expected for gas exposed to a continuous ram pressure force (Köppen et al. 2018). This implies that some of the difference between the analytic model and simulation in panel (a) is due to differing definitions of “stripped” gas.



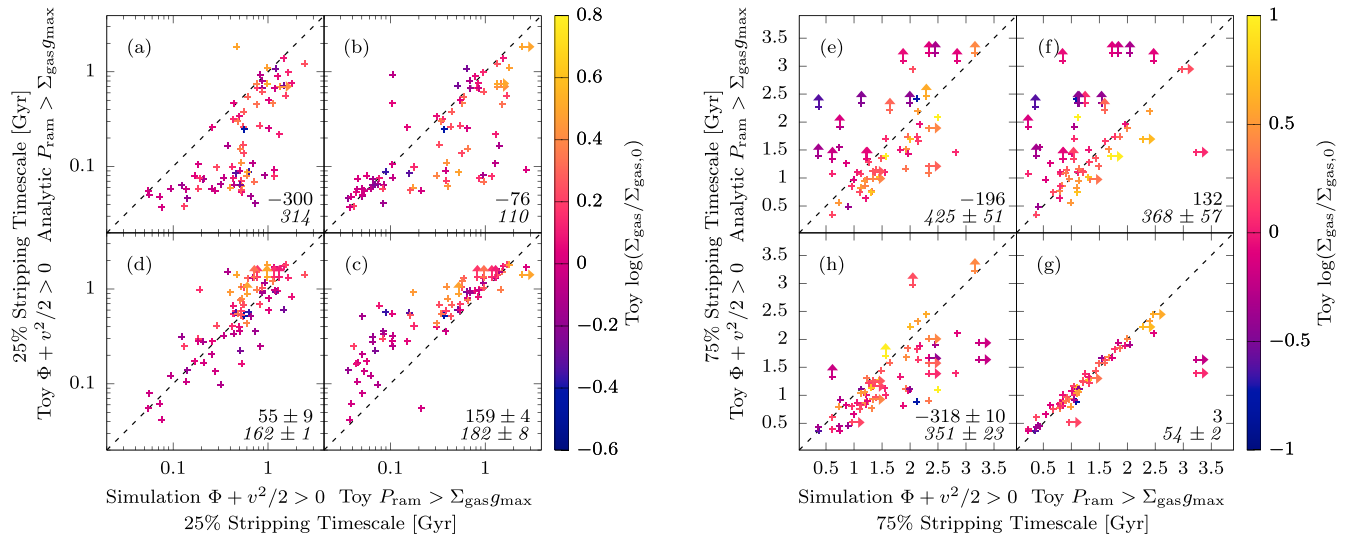


**Figure 5.** Gas stripping timescales for the ionized gas in our galaxy sample, given by the simulation as well as by the analytic and toy models described in Section 3. Panels (a)–(d) on the left show the timescale at which 25% of the ionized gas mass is stripped, whereas panels (e)–(h) on the right show the timescale at which 90% is stripped. Note that the left panels are in log scale as there is a large range in timescales. As our simplified models contain no prescription for star formation, we remove those gas particles that have transformed into star particles by the next simulation output from consideration when computing stripped fractions. The color scale in the panels represents  $\Sigma_{\text{gas}}/\Sigma_{\text{gas},t=0}$  for each galaxy, i.e., the median ratio of the surface density relative to its value at the initial time in the toy model. This is computed at the time when the toy model reaches the presented unbound fraction (25% or 90%). Where the toy model fails to ever reach the latter fraction, the value of  $\Sigma_{\text{gas}}/\Sigma_{\text{gas},t=0}$  at the final output is shown. Arrows indicate lower limits (where a model or the simulation does not reach the given stripped fraction), but galaxies in which neither the  $x$ -axis nor  $y$ -axis value achieves the given stripped fraction are excluded from the plot. The numbers in the bottom-right corner of each panel give the median deviation and median absolute deviation (italics) of the  $y$ -axis timescale from the  $x$ -axis timescale, in megayears. Due to the presence of lower limits, the median is sometimes not uniquely determined. In these cases, we give the possible range of the median value.

Additionally, for the 25% timescale for the ram pressure force to exceed the maximum restoring force, there are differences between the analytic model and toy model. This is shown in panel (b). Here the analytic model predicts a stripping timescale slightly shorter than the toy model, by 76 Myr.

From these panels we find that there is good agreement between the toy model and simulation predictions for the 25% stripping timescale (panel (d)). We also see that the timescale predicted by the analytic model from McCarthy et al. (2008) is shorter than that from the simulation (panel (a)), which is partly due to the fact that it takes longer for gas to become energetically unbound than it does for it to encounter the maximum restoring gravitational acceleration during its orbit (panel (c)). However, even the analytic timescale to reach the maximum restoring acceleration is not fully in agreement with that predicted by the toy model (panel (b)). This is partly due to the fact that the analytic prescription does not include evolution of the gas mass surface density,  $\Sigma_{\text{gas}}$ . Based on Figure 4, we expect the evolution of  $\Sigma_{\text{gas}}$  to generally increase the predicted stripping timescale in the toy model relative to the analytic model, and we check this by color-coding each galaxy by its change in  $\Sigma_{\text{gas}}$ .

The color scale in panels (a)–(d) represents the same quantity shown in Figure 4 for the toy model—the median of the ratio of each gas particle’s  $\Sigma_{\text{gas}}$  to its initial value—at the 25% unbound timescale of the toy model for each galaxy. We see in panel (b) that galaxies whose ionized gas tends to increase in surface density also tend to have longer stripping timescales than the analytic model, which does not include evolution of  $\Sigma_{\text{gas}}$ .

Panels (e)–(h) in Figure 5 are similar to panels (a)–(d) except that they show the timescale at which 90% of the ionized gas is stripped from each galaxy in the simulation, toy model, and

analytic model. Unlike for the 25% stripping timescale, there does not appear to be a significant difference between the energetic and force-based criteria for stripping in the toy model, as seen in panel (g). There is again some disagreement between the toy model and analytic model, as seen in panel (f), though now the analytic model is typically longer than the toy model (median deviation 132 Myr). There is also a substantial scatter between the two models ( $\approx 368$  Myr) that has the expected correlation with the evolution of  $\Sigma_{\text{gas}}$  in the toy model (color scale).

Both the analytic and toy models underestimate the 90% stripping timescale from the simulation, as seen in panels (e) and (h). The scatter between the analytic model and simulation in panel (e) correlates with the evolution in  $\Sigma_{\text{gas}}$  in the same way as the scatter between the analytic and toy models in panel (f), suggesting that the evolution in  $\Sigma_{\text{gas}}$  genuinely influences the ram pressure stripping rate.

Figure 6 has a similar format to Figure 5 but presents the results for the neutral gas. The left four panels show the 25% stripping timescales from the models and simulation, while the right panels show the same for the 75% stripping timescale. Unlike for the ionized gas, the 90% timescale is not shown, as the majority of the galaxies do not reach this level of stripping of their neutral gas.

We see in panel (c) of Figure 6 that the timescale for 25% of the neutral gas particles to become gravitationally unbound is slightly longer than the same timescale for exceeding the maximum restoring acceleration, with a median deviation of 43 Myr. For the 75% timescale, in panel (g), the difference is negligible. In addition to there being little difference between the two definitions for stripping, the analytic model is in approximate agreement with the toy model for both the 25% and 75% stripping timescale (panels (b) and (f), respectively).

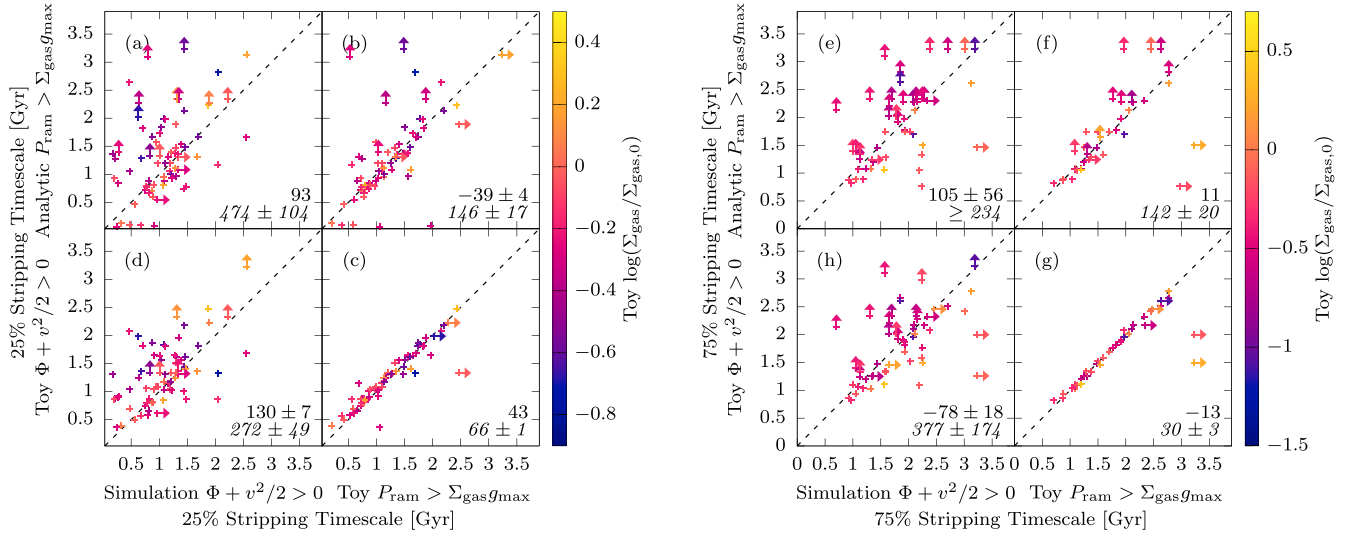


**Figure 6.** The same as Figure 5, except all values are shown for the neutral gas, and the timescale shown in panels (e)–(h) is for stripping of 75% of the gas, as the neutral disk is not stripped of 90% of its gas for most of the galaxies in the toy model and analytic approximations.

The majority of the differences between the analytic model and the simulation, seen in panels (a) and (e), are also present in the toy model, seen in panels (d) and (h). The toy model overestimates the timescale for 25% of the gas to become unbound by on average (median)  $\approx 130$  Myr, and there is a significant scatter ( $\approx 272$  Myr) between the toy model and simulation timescales as well. While the median difference in the 75% stripping timescale between the toy model and the simulation is only 78 Myr, the median absolute deviation between the two is significant, being  $377 \pm 174$  Myr.

Additionally, in contrast to the ionized gas, there is no correlation between the evolution in the gas mass surface density and the difference between the analytic and toy models. This may be because the evolution in  $\Sigma_{\text{gas}}$  is insufficient to significantly change the neutral gas disk stripping timescales in the toy model, as the toy model is nearly always in good agreement with the analytic model (panels (b) and (f)).

We now check that the trends seen in Figures 5 and 6 are not somehow artifacts of the definition used for “stripping.” Observations of gas stripping in galaxies are generally based on physical separation of gas from the body of the galaxy, rather than gravitational binding, which is not directly observable. Thus, in Figure 7, we present results for stripping based on the assumption that a particle is “stripped” when it exits the initial 99% radius of either the neutral disk or ionized halo (depending on which it originally belongs to). We show a comparison only between the toy model and simulation as the analytic model does not allow us to predict the locations of particles.

The left panels of Figure 7 show the 25% and 90% stripping timescales for the ionized gas using the above definition of stripping, and the right panels show the 25% and 75% stripping timescales for the neutral gas. The trends are highly similar to those seen when comparing the toy model to the simulation in Figures 5 and 6. There is good agreement for the 25% stripping timescale of the ionized gas, but the 90% timescale is significantly underestimated by the toy model. In contrast, the 25% stripping timescale for the neutral gas is overestimated by the toy model, and there is significant scatter between the toy model and simulation predictions of the 75% stripping

timescale for the neutral gas, although the median deviation between the two is small (59 Myr).

In this subsection, we have examined the differences in the stripping timescales predicted by the analytic ram pressure stripping models, our toy model, and the EAGLE simulation. For the 25% stripping timescale of the ionized gas, which is often short (a few hundred megayears), we find that the toy model agrees with the EAGLE simulation, but the analytic model does not. The latter is due to the fact that the definition of stripping in the analytic model differs from that in the simulation, and also because the analytic model somewhat underestimates the stripping timescale relative to the toy model even using the same definition of stripping.

However, for the 90% stripping timescale of the ionized gas, as well as both the 25% and 75% stripping timescales of the neutral gas, the above two factors become negligible, and the differences between the analytic model and simulation are paralleled in the differences between the toy model and simulation. Both the analytic and toy models predict 90% stripping timescales that are too short for the ionized gas, 25% stripping timescales that are too long for the neutral gas, and 75% stripping timescales for the neutral gas that have a significant scatter between their values and those of the simulation. We will explore the reason for these seemingly disparate trends in the next subsection.

## 5. Toy Model Deviations from the Simulation

In this section, we examine the hydrodynamical and subgrid effects that are present in the EAGLE simulation but not the toy model, and cause the latter to deviate from the former. The important factors that we identify are stellar feedback, the cooling of ionized gas into denser neutral gas, and the fact that the gas appears to be confined by an additional hydrodynamical force that increases with ram pressure. As shown in Section 4, the differences in stripped gas fraction between the toy model and simulation also constitute the majority of the difference between the results of the analytic models and those of the simulation.

Unlike in Section 4.1, in this section we show the results of the toy model run over the time between each two subsequent simulation outputs (typically  $\approx 120$  Myr). This is summarized

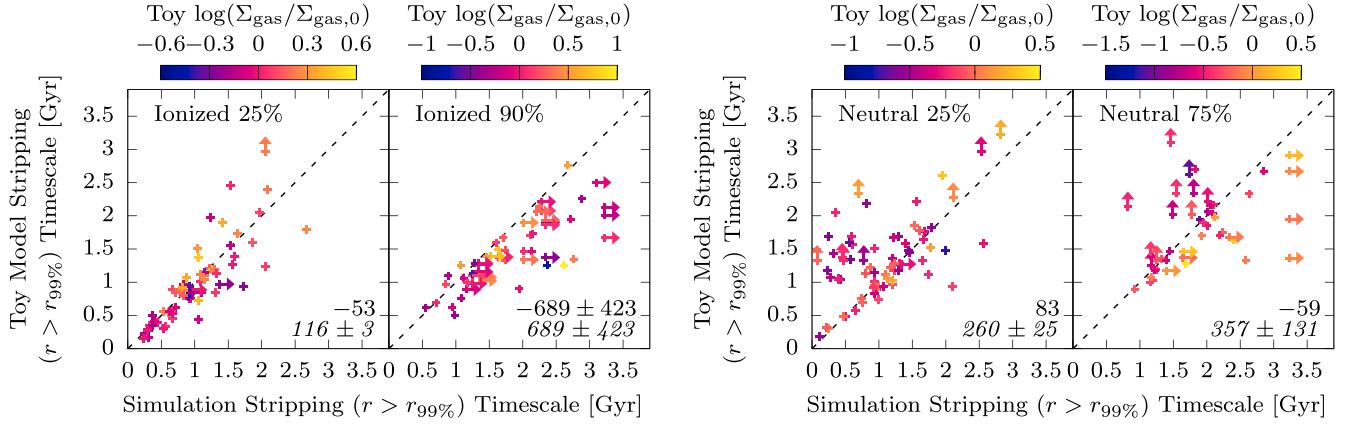


**Figure 7.** Like panels (d) and (h) in Figures 5 and 6, this figure shows the stripped fraction in the toy model vs. that in the simulation, except here to be “stripped” means to exit the radius initially containing 99% of the gas in the disk or halo, rather than to be energetically unbound. From left to right, the panels represent the timescales for 25% and 90% of the gas to be stripped from the ionized halo and 25% and 75% of the gas to be stripped from the neutral disk.

in Table 2 as the “single-step” toy model. We do this because the toy model is simplified and will thus diverge from the simulation over time, and so examining the difference between the toy model and simulation over shorter timescales makes it easier to identify the physical processes in the simulation that cause it to differ. Our “single-step” analysis results in a total of 1383 outputs for the 80 galaxies in our sample, each of which is treated as an independent data point.

While we once again divide the gas into neutral and ionized components, we now do this at each output rather than only when we begin tracking the galaxy. Furthermore, the ability of gas to transition between phases constitutes one of the important differences between the simulation and toy model. We thus divide gas into four categories in this section rather than two: gas that is neutral in the subsequent simulation output, which we denote “NN” in the text for brevity; gas that is ionized in both simulation outputs (“II”); gas that is initially neutral and becomes ionized in the next simulation output (“NI”); and gas that transitions from ionized to neutral (“IN”).

In the rightmost panel of Figure 8, we show the gas mass fraction in each of these four categories per individual output as a function of ram pressure. The lines with error bars denote the median and interquartile range.

At negligible ram pressures ( $P_{\text{ram}} \lesssim 10^{-15}$  Pa), when the galaxies first begin their journey into the cluster, the majority ( $\approx 75\%$ ) of the gas bound to each galaxy is ionized and remains so (II), while the next largest fraction of gas ( $\approx 25\%$ ) is neutral and remains so (NN). The fraction of II gas drops to only a few percent at high ram pressures ( $P_{\text{ram}} \gtrsim 10^{-12}$  Pa), while NN gas becomes the dominant type of gas bound to the galaxy ( $\approx 90\%$  mass fraction).

Gas that is ionized and becomes neutral (IN) is generally of the order of 1% of the gas mass at all ram pressures. However, over the full evolution of the galaxy in cluster, a substantial fraction of the initially ionized gas can be converted to neutral gas. We find that a median of 33% of the initially ionized gas becomes neutral at some point (interquartile range 17%–50%), although some of this gas may become ionized again later. This plays a role in why the toy model overpredicts the stripping of the initially ionized gas, as seen in Figure 5. Some of this ionized gas cools to become denser neutral gas, which is more difficult to strip.

By contrast, gas that is initially neutral but becomes ionized (NI) increases in the fraction of total mass it comprises from

$\approx 1\%$  at low ram pressures to  $\approx 10\%$  at the highest ram pressures. Like for the IN gas, there is significant conversion over time from neutral to ionized gas: the median fraction of initially neutral gas converted to ionized gas at some point is 51% (interquartile range 41%–58%). NI gas is associated with stellar feedback, which we will discuss further in Section 5.1.

In the left four panels of Figure 8, we show, for each of these four categories of gas, the single-step unbound gas fraction as a function of ram pressure. The green solid lines represent the median and quartiles of the unbound gas fraction in the simulation. The same is shown for the toy model as light-blue dashed lines. The points show the difference between the unbound fraction in the simulation and toy model for each galaxy at each output, with the color representing the stripped fraction in the simulation.

The top-left panel of the left side of Figure 8 plots the unbound fraction of II gas. We see that the toy model gives a similar increasing trend with ram pressure as the simulation, but predicts slightly too much stripping (by  $\lesssim 10\%$ ) at ram pressures  $\gtrsim 10^{-13}$  Pa. The IN gas is shown in the bottom-left panel, and in contrast to the II gas, the toy model significantly overpredicts the unbound gas fraction at  $\gtrsim 10^{-13}$  Pa. As noted above, this is partly due to the fact that this ionized gas cools and becomes denser—a hydrodynamical effect that is not included in the simple toy model. Both of these effects are in agreement with the results found for the ionized gas in the long-timescale integration shown in Figure 5, in which the toy model at low ram pressures matches the simulation, but tends to underpredict stripping timescales at high ram pressures.

The top-right panel in the collection of four panels seen in the left of Figure 8 shows the NI gas. Here, the simulation stripped fraction is larger than that from the toy model at all ram pressures, even negligible ones. As we will discuss further in Section 5.1, this is consistent with the effect of stellar feedback, which is implemented as stochastic and thermal in EAGLE.

Finally, the bottom-right panel of the left portion of Figure 8 shows the NN gas. As noted above, this category of gas is dominant at high ram pressures, where most of the ionized gas has already been stripped. The NN gas generally has a low stripping rate even at the highest ram pressures, although there are galaxies where nearly all of the gas is stripped in the simulation (appearing as yellow points). At high ram pressures ( $P_{\text{ram}} \gtrsim 10^{-12}$  Pa), the toy model overpredicts the median



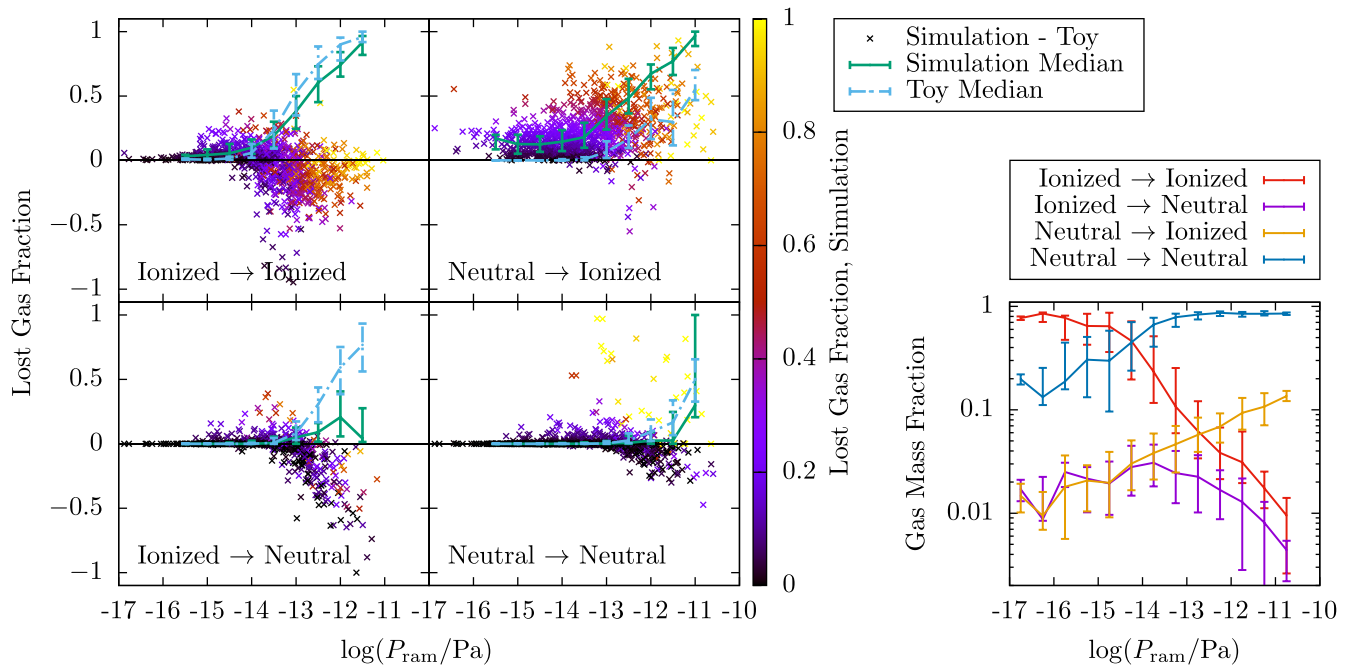


**Figure 8.** Left four panels: the fraction of gas mass unbound from each galaxy in the toy model and simulation between two simulation outputs (typically  $\approx 120$  Myr), as well as the difference between the two models. The top-left panel shows these values for gas that is ionized at both the presented and subsequent simulation output (denoted “II”). The top-right panel presents gas that is initially neutral but becomes ionized (“NI”), the bottom-left panel shows ionized gas that becomes neutral (“IN”), and the bottom-right panel shows gas that is neutral and remains so (“NN”). In each panel, the solid green line denotes the median and quartiles of the distribution of unbound gas fraction in the simulation as a function of instantaneous ram pressure. The light-blue dashed line is the same but for the prediction of the toy model. The points in each panel represent the unbound fraction from the simulation minus that from the toy model for each output for each galaxy. A simulation output is only included in this figure if a galaxy has at least 20 particles of a given type at that time. The color of each point represents the unbound fraction from the simulation for that output and galaxy. Right panel: the mass fraction of each category of gas as a function of ram pressure: the red line is II gas, purple is IN, orange is NI, and blue is NN. Lines denote median values, and error bars denote quartiles.

stripped fraction of this category of gas, but the interquartile range of the stripped fraction is significantly larger in the simulation. In the next two subsections, we will argue that this is due to the combined effect of feedback from stars, and the action of a confining force on the galactic gas.

### 5.1. Effect of Stellar Feedback

One factor that can contribute to excess gas loss in the simulation, particularly in the neutral gas disk, is feedback. We find that in our galaxy sample, there is little supermassive black hole growth compared to star formation, and the thermal energy added to the galactic gas correlates well with the number of star particles formed but not with the black hole accretion rate. Stellar feedback appears to be the main feedback source for galaxies in our sample, and we thus focus here on feedback from newly formed star particles.

In EAGLE, feedback is implemented as purely thermal and stochastic, such that some gas particles around a newly formed star particle have their temperature raised by  $10^{7.5}$  K. The pressure gradient generated by this influx of energy then drives a wind in the gas (Mitchell et al. 2020). Thus, the regions around newly formed star particles should exhibit a significant excess of kinematically unbound particles. The thermal energy should also be transferred among nearby gas particles and cause some neutral particles to become ionized. Feedback should also act even at low ram pressures, as star formation is present in the absence of ram pressure. This could therefore account for the trend seen in the NI gas in Figure 8, whose rate of kinematic unbinding (which does not take into account

thermal energy) is underestimated by the toy model even at negligible ram pressures.

We further examine the effects of stellar feedback in Figure 9. In the left four panels, we compare the spatial distribution of the four gas categories seen in Figure 8 as a function of average distance from newly formed star particles in their galaxies. This was computed by stacking all of the new star particles expected to undergo feedback between simulation outputs, and averaging the cumulative fraction of total gas around them as a function of distance. (The positions used are the initial positions of all particles rather than evolved ones at the moment of feedback; thus, the correlation may be decreased relative to its true strength.) The stacked means are then averaged over all outputs/galaxies. Error bars represent the errors on the mean.

The four panels in the left panels of Figure 9 represent bins of different ram pressure, while the colored lines represent the four gas categories (II, NI, IN, and NN). We see that at all ram pressures, the initially neutral gas—both NN and NI gas—is closer to regions that are forming stars than the initially ionized gas. This is expected, as stars form in dense gas in EAGLE. The IN gas is closer to the star-forming regions than the II gas, particularly at low ram pressures. This is likely because the ionized gas that becomes neutral is that closest to the neutral gas disk, and cools onto it. Overall, we would expect a larger fraction of the total neutral gas to be affected by stellar feedback than the ionized gas, simply due to the greater proximity of the neutral gas to newly formed star particles.

We also note that both the neutral and ionized gas distributions become closer to newly formed star particles on average with increasing ram pressure. This is partly because

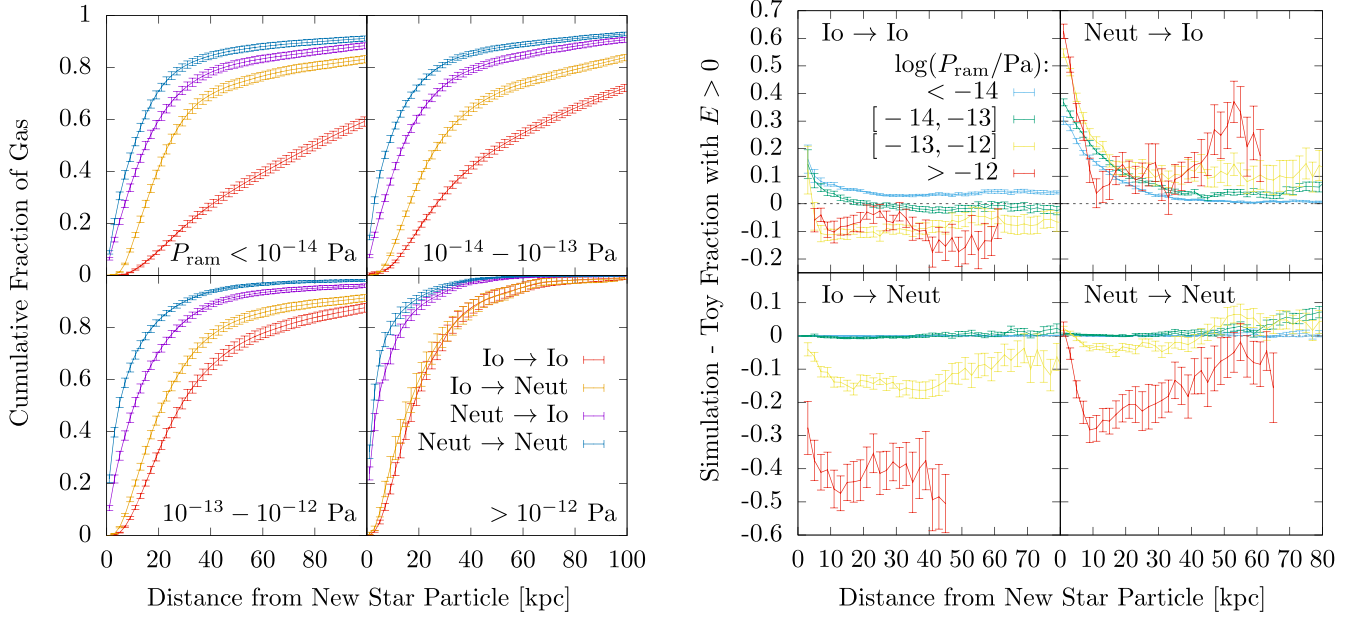


**Figure 9.** Left four panels: the mean cumulative fraction of gas in EAGLE galaxies as a function of distance from newly formed star particles. Different colored lines represent different categories of gas, with the colors and categories being the same as for the right panel of Figure 8. The different panels represent bins of increasing ram pressure. Error bars are the error on the mean. Right four panels: the difference between the fraction of gas unbound in the simulation and that unbound in the toy model, as a function of distance from newly formed star particles. The four panels represent the four different categories of gas. The colors represent increasing bins of ram pressure: light blue is  $P_{\text{ram}} < 10^{-14}$  Pa, green is  $10^{-14}$  Pa  $< P_{\text{ram}} < 10^{-13}$  Pa, yellow is  $10^{-13}$  Pa  $< P_{\text{ram}} < 10^{-12}$  Pa, and red is  $P_{\text{ram}} > 10^{-12}$  Pa. Error bars are the error on the mean. Bins in which fewer than 10 galaxies have any gas particles are not shown.

diffuse gas far from the neutral disk is already stripped at high ram pressures, but also partly because the force of ram pressure tends to compress gas—which also triggers increased star formation (Troncoso-Iribarren et al. 2020).

In the four right panels of Figure 9, we plot the mean difference between the unbound gas fraction in the simulation and that predicted by the toy model as a function of distance from newly formed star particles. The average is computed in the same manner as for the cumulative fraction of gas in the left panels, described above. Here the different panels show the four different categories of gas, while the different line colors indicate bins of different ram pressure. Since feedback in EAGLE is implemented as a temperature increase in gas particles close to newly formed star particles, we would expect feedback-related differences between the simulation and toy model to be correlated with the locations of the newly formed star particles.

The top-right panel shows NI gas, which we would expect to result from the thermal energy that is injected by feedback in EAGLE. We emphasize that the unbound gas fractions presented in this figure are based solely on the sum of the kinetic and potential energy of the gas particles, and do not include the thermal energy. We see that NI gas particles close to newly formed star particles are significantly more likely to have a velocity higher than the escape speed in the simulation than in the toy model. The correlation with the location of newly formed star particles is evident in all ram pressure bins. Furthermore, at higher ram pressures, the difference in unbound fraction between the simulation and toy model is larger. This implies that ram pressure assists feedback in expelling gas from galaxies.

In the bottom-right panel of the four right panels of Figure 9, we plot the same quantity described above but for the NN gas. Here there is little difference between the simulation and toy model for  $P_{\text{ram}} \lesssim 10^{-13}$  Pa. As seen in Figure 8, at these low

ram pressures, very little NN gas becomes unbound in either model. At higher ram pressures, however, we see two effects. The difference between the simulation and toy model unbound fraction is enhanced relative to the baseline value closer to newly formed star particles, but the overall stripped fraction in the simulation is lower than that in toy model. We will discuss the reason for the latter in Section 5.2. Nevertheless, the fact that Figure 9 is an average over all galaxies suggests that it is consistent with Figure 8 for the NN gas: some galaxies at high ram pressure have NN gas that is significantly unbound by feedback, whereas in others the overall underprediction of stripping by the toy model relative to the simulation is the dominant effect.

In the bottom-left panel of the right set of panels in Figure 9, we see the same types of curves as described above but for IN gas. Like for the NN gas, at  $P_{\text{ram}} \lesssim 10^{-13}$  Pa there is no significant difference between the simulation and toy model. This is also visible in Figure 8, where both models generally predict no stripping at these ram pressures. At higher ram pressures, we see similar trends as for the NN gas, but there is an even larger overall negative difference in the stripped gas fraction between the simulation and the toy model. This is because the ionized gas becomes more dense when it becomes neutral, which makes it more resistant to stripping, an effect not accounted for in the toy model. We will discuss this in more detail in Section 5.2.

Finally, in the top-left panel of the right half of Figure 9, we show the results for the II gas. Here the unbound fraction is again higher than the baseline close to newly formed stars (except in the highest ram pressure bin, for which there is not enough data at small distances). Similar to the IN and NN gas, the overall level of stripping in the simulation relative to the toy model decreases with increasing ram pressure. In the lowest ram pressure bin, there is a constant low fraction of lost ionized

gas that may be due to stochastic unbinding of these very weakly bound gas particles.

Although the II gas and IN gas are locally affected by feedback at small distances from newly formed star particles, they will be less affected overall than the NN and NI gas. This is because the majority of all II and IN gas is located at larger distances from stellar feedback regions than NN and NI gas, as can be seen in the left half of Figure 9.

The differences between the simulation and toy model for the different categories of gas presented in Figure 9 explain a number of the trends seen in Figure 8. The NI gas is the category of gas that is most strongly affected by stellar feedback, and thus is stripped more in the simulation than in the toy model at all ram pressure values. For the other gas categories, the simulation sometimes predicts more stripping than the toy model, but more often it predicts less stripping, especially at high ram pressures. This can be seen in Figure 9 as a negative difference between the simulation and toy model stripped gas fractions far from regions that are undergoing stellar feedback. In the following section, we will discuss the reasons that the simulation predicts less stripping than the toy model at high ram pressures.

### 5.2. Influence of Gas Mass Surface Density

We have seen in Figure 9 that, away from galactic regions strongly affected by stellar feedback, the toy model increasingly overpredicts the fraction of unbound gas with increasing ram pressure. A significant cause of this is underprediction of the gas mass surface density by the toy model. This is presented in Figure 10, which shows the ratio of toy model to simulated predicted gas mass surface density,  $\Sigma_{\text{gas}}$ , perpendicular to the ram pressure direction. The toy model prediction uses the positions and velocities of the galaxy gas particles in each simulation output, as well as the ram pressure and subhalo potential, to predict their positions in the next simulation output. This predicted gas distribution is used to calculate the toy model  $\Sigma_{\text{gas}}$  at the location of each gas particle. The simulation  $\Sigma_{\text{gas}}$  is computed from the true final positions of the gas particles in the simulation. The ratio between the toy model and simulation  $\Sigma_{\text{gas}}$  for each output/galaxy is shown as the light-blue points in Figure 10, while the median and quartiles of their distribution in bins of ram pressure are represented by the dark-blue lines. We note that  $\Sigma_{\text{gas}}$  is computed using all of the gas present in the galaxy in the initial simulation output, regardless of gas phase: each gas component contains the density contribution of the other components that are in its line of sight.

Different behavior can be seen for different categories of gas in Figure 10. For the NI gas, seen in the top-right panel of Figure 10, the toy model nearly always predicts higher gas mass surface densities than the simulation. This is unsurprising, as the NI gas is associated with stellar feedback events, which are not accounted for in the toy model and induce a wind in the gas, causing the gas mass surface density to become lower.

For the II gas in Figure 10, we see that the median ratio between the toy model gas surface density and that in the simulation tends to be close to one, although at high ram pressures, some galaxies have significantly lower densities in the toy model than in the simulation. The latter effect is even more pronounced for the NN and IN gas, for which the toy model strongly underpredicts the gas mass surface density at high ram pressures.

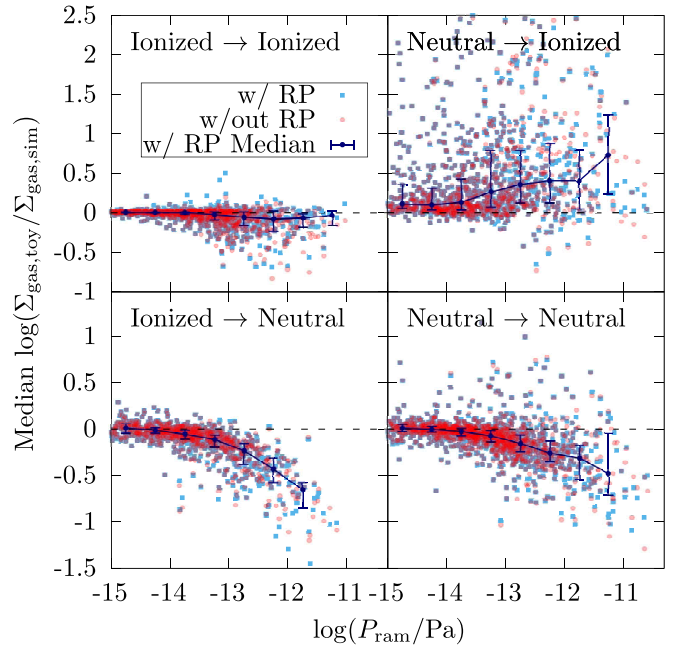


**Figure 10.** The median ratio between the toy model and simulation predictions for the gas mass surface density  $\Sigma_{\text{gas}}$  perpendicular to the ram pressure, as a function of ram pressure. Each point represents a single galaxy between two subsequent simulation outputs. The light-blue points show the ratio predicted by the toy model with ram pressure included, while the red points are for the toy model integration assuming zero ram pressure. The dark-blue lines represent the median and quartile values of the distributions of the light-blue points. In each panel, the only outputs shown are those in which the galaxy has at least 20 particles of the given gas category. The values of  $\Sigma_{\text{gas}}$  are computed using all of the gas particles bound to the subhalo at each starting output, regardless of whether they are unbound by the subsequent output. The four different panels present the same four gas categories shown in Figures 8 and 9.

We emphasize that none of the trends seen in Figure 10 are the result of differing amounts of gas being stripped in the toy model versus the simulation. This is because the values of  $\Sigma_{\text{gas}}$  used to create Figure 10 are computed using all of the gas particles that are initially bound to the subhalo, regardless of whether they have become unbound in the subsequent simulation output. Thus, the difference in  $\Sigma_{\text{gas}}$  is due to the different final positions of the gas particles predicted by the toy model and simulation, rather than due to particles being excluded due to becoming unbound. For the NN and IN gas especially, the toy model predicts a gas distribution that is more diffuse in the direction perpendicular to the ram pressure than the simulation.

The results seen in Figure 10 are similar to those seen in Figure 4, which presented the evolution of  $\Sigma_{\text{gas}}$  for only the bound particles remaining at each time during the long-timescale integration. In Figure 4,  $\Sigma_{\text{gas}}$  of both the initially ionized and initially neutral gas became higher in the simulation than in the toy model. In the simulation, some of the initially ionized gas will become neutral, and therefore denser and less likely to be unbound than gas that remains ionized. From this alone, we would expect the initially ionized gas that remains in the galaxy to be denser than is predicted from the toy model, because some of it has since become neutral. However, in addition to this, once the gas has become neutral, NN gas is more dense in the simulation than predicted by the toy model, as seen in Figure 10. Conversely, NI gas becomes less dense, but is more likely to be stripped from the galaxy than initially neutral gas that remains neutral. Thus, it is



expected that both the initially ionized and initially neutral gas that remain bound to the galaxy are denser in the simulation than in the toy model.

Because ram pressure moves gas to the outer, less-bound regions of the subhalo, it can cause the distribution of gas to expand in the perpendicular direction. Thus, adopting an overly large value for the ram pressure in the toy model could theoretically cause the gas surface density in the toy model to be lower than in the simulation. However, we demonstrate that this *not* the cause of the discrepancy via the red points in Figure 10. These show the ratio of the toy model to simulated  $\Sigma_{\text{gas}}$  for a toy model in which the ram pressure is set to zero: the gas particles are simply evolved from their initial positions and velocities under the gravitational potential of the subhalo. We see that the values of  $\Sigma_{\text{gas}}$  predicted by this model are still smaller than the values from the simulation.

Since the gas in simulated galaxies is more compact than predicted by the toy model, it will be more resistant to ram pressure than expected, leading to lower stripped gas fractions. This is a significant cause of the lower stripping rate in the simulation compared to the toy model noted in Figures 8 and 9 at high ram pressures for II, NN, and IN gas.

We would like to further examine the different predictions made for the gas mass surface density  $\Sigma_{\text{gas}}$  in the toy model and simulation. We thus present the average evolution of  $\Sigma_{\text{gas}}$  between two subsequent simulation outputs for the NN, IN, and II gas in Figure 11. The evolution is shown as the difference between the final and initial mean  $\log(\Sigma_{\text{gas}})$ , for both the toy model (without ram pressure) and the simulation, as a function of radius perpendicular to the ram pressure (scaled by the initial 90% radius). The initial and final mean values of  $\log(\Sigma_{\text{gas}})$  are computed as an average over all of the gas particles in each radial bin, using all gas particles that were bound to the galaxy at the initial simulation output. The values of  $\Sigma_{\text{gas}}$  are thus averaged per gas particle, rather than per unit area, meaning that an increase in  $\Sigma_{\text{gas}}$  at all radii indicates an increase in the clustering of gas particles at all radii.

We associate IN gas with an increase in density due to cooling, and this is indeed what is seen in the center column of Figure 11. The toy model  $\Sigma_{\text{gas}}$  does not evolve significantly between two simulation outputs, but  $\Sigma_{\text{gas}}$  in the simulation increases at all radii. The disparity between the simulation and toy model increases with ram pressure.

By contrast, in the left column of Figure 11 showing the NN gas,  $\Sigma_{\text{gas}}$  from the simulation does not evolve significantly, while  $\Sigma_{\text{gas}}$  in the toy model tends to decrease between two simulation outputs. The discrepancy between the simulation and toy model increases with radius and with ram pressure. This trend suggests a confining force acting on the gas whose strength is correlated with the ram pressure.

While most outputs/galaxies show little difference between the toy model and simulation for the predicted  $\Sigma_{\text{gas}}$  of the II gas, we would like to examine the evolution of  $\Sigma_{\text{gas}}$  for those outputs where there is a discrepancy between the two. Thus, the right column of Figure 11 shows the II gas, but only for those outputs/galaxies that fall below the median trend of  $\Sigma_{\text{gas,toy}}/\Sigma_{\text{gas,sim}}$  with ram pressure. Here the II gas demonstrates a trend more similar to the NN gas than the IN gas:  $\Sigma_{\text{gas}}$  does not evolve significantly in the simulation, but tends to decrease in the toy model.

Figure 11 suggests a confining force on the galaxy gas that acts in addition to the force of the gravitational potential of the

subhalo, which is accounted for in the toy model. We find that the self-gravity of the galaxy gas, which is not accounted for in the simple toy model, is not sufficient to explain the additional force. Nor is the force caused by unaccounted-for changes in the subhalo potential, as we have run our toy model integration (without ram pressure) on the collisionless stellar particles, finding that their predicted positions are in good agreement with those from EAGLE. This implies that the confining force seen in Figure 11 is hydrodynamical in nature. While the thermal confinement pressure of the surrounding ICM could potentially produce the observed confinement effect, we do not find a correlation between  $\Sigma_{\text{gas,toy}}/\Sigma_{\text{gas,sim}}$  and the ICM confinement pressure at fixed ram pressure, although there is a correlation between  $\Sigma_{\text{gas,toy}}/\Sigma_{\text{gas,sim}}$  and ram pressure at fixed confinement pressure. This suggests that the observed confining force may be somehow related to the ram pressure force.

Additionally, we have run our toy model without ram pressure on a sample of cluster galaxies from the Illustris TNG 100 Mpc simulation, chosen in a similar manner as our EAGLE galaxy sample. We find the same result regarding the galactic gas being more compact than expected at high ram pressure that we see in EAGLE. Therefore, this effect does not appear to result from the specific hydrodynamic scheme used in EAGLE.

As the difference in  $\Sigma_{\text{gas}}$  between the toy model and simulation correlates strongly with ram pressure, we suggest that its cause may be deflection of the ICM wind by the galactic gas. The standard Gunn et al. (1972) formula for the ram pressure,  $P_{\text{ram}} = \rho_{\text{ICM}} v_{\text{rel}}^2$ , assumes that all of the momentum of the ICM wind is transferred to the galactic gas. However, ICM particles tend to be deflected around the galaxy in the simulation, such that they do not deposit all of their momentum into the galaxy gas. Such a deflection will tend to produce an inward force on the galactic gas that increases  $\Sigma_{\text{gas}}$ , and also to decrease the force exerted in the assumed ram pressure direction, which will further decrease the stripping rate relative to the toy model prediction. We would expect the magnitude of the confinement from this effect to increase with ram pressure, although it will also depend on the geometry of the galaxy gas. We demonstrate the deflection of ICM particles around an example galaxy in Figure 12.

### 5.3. Discussion of Toy Model Deviations

We have seen in this Section that there are multiple hydrodynamical effects that alter the stripping rate of gas from ram pressure stripped galaxies. One is that gas is able to transition between neutral and ionized and this affects a significant fraction of the initially bound gas. Initially ionized gas can cool and become denser and more difficult to strip, as is demonstrated in the “Ionized  $\rightarrow$  Neutral” panels in Figures 10 and 11. Similarly, neutral gas can become ionized and decrease in density, seen in the “Neutral  $\rightarrow$  Ionized” panel of Figure 10. The fraction of total gas undergoing each of these two processes at each simulation output can be seen as a function of ram pressure in the rightmost panel of Figure 8.

The transformation of neutral gas to ionized is associated with stellar feedback, which significantly alters the stripping rate by inducing a pressure-driven wind in the gas. In the right four panels of Figure 9, this can be seen as a larger local fraction of stripped gas in the simulation than the toy model close to newly formed star particles. This is most readily seen in the top-right panel for the neutral gas that becomes ionized, which we would expect to be associated with the thermal

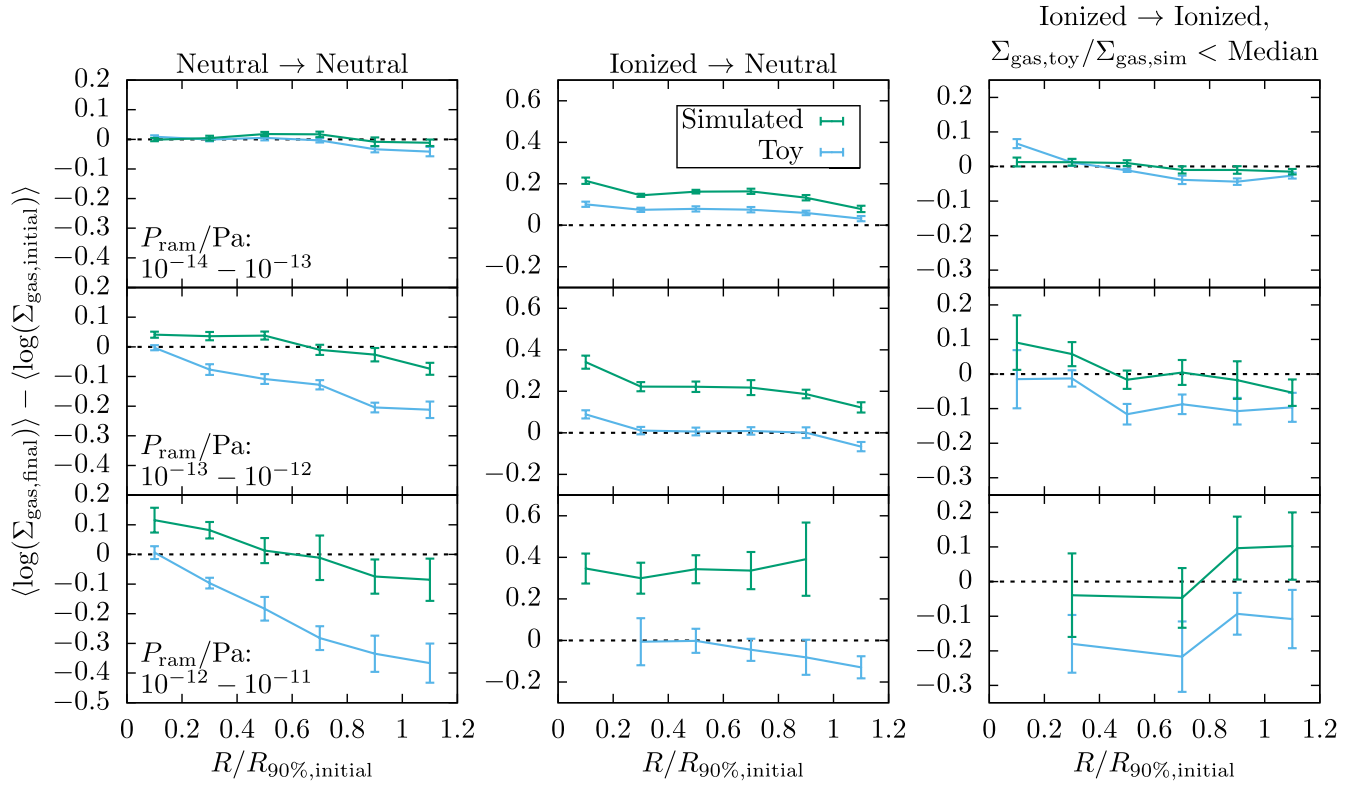


**Figure 11.** The evolution of  $\Sigma_{\text{gas}}$ , the gas mass surface density perpendicular to the ram pressure, as a function of the radius perpendicular to the ram pressure  $R$ , scaled by the 90% value of  $R$  at the initial simulation output (computed separately for the different categories of gas). The evolution of  $\Sigma_{\text{gas}}$  is expressed as the difference between the final and initial mean  $\log(\Sigma_{\text{gas}})$  of the gas particles in each radial bin for each galaxy. This is averaged over all of the galaxies in a bin of ram pressure. The green lines represent the evolution of  $\Sigma_{\text{gas}}$  from the EAGLE simulation, whereas the light-blue lines represent the evolution predicted by the toy model without ram pressure (see the text). The rows indicate bins of increasing ram pressure, while the columns represent three categories of gas: NN, IN, and II. The II gas is averaged over only the galaxies that fall below the median relation of  $\Sigma_{\text{gas,toy}}/\Sigma_{\text{gas,sim}}$  as a function of ram pressure. Galaxies/outputs included in the average are those with at least 20 gas particles of the indicated type. Error bars represent errors on the mean.

feedback implementation in EAGLE. However, it is also visible as an increase over the baseline difference between the simulation and toy model stripping rate for all four categories of gas presented. The stripping enhancement caused by the feedback becomes more pronounced with increasing ram pressure, implying that the ram pressure and feedback work in tandem to unbind gas from the galaxy.

That ram pressure and stellar feedback work together to unbind more gas than either would individually is in agreement with previous results obtained by Bahé & McCarthy (2015) using the GIMIC simulation, even though the implementation of feedback in their simulation was kinematic rather than thermal. That galaxies continue to form stars while they are being ram pressure stripped is also consistent with results from the Illustris TNG simulations (Göller et al. 2023).

We note, however, that our analysis likely overestimates the impact of stellar feedback on ram pressure stripped galaxies, as it has been found that stellar feedback in EAGLE is too strong due to the limited resolution of the simulation. Because the mass of a star particle in EAGLE is much larger than a single star, there is too much feedback energy injected into a small region of the galaxy, leading to unphysically large holes in the neutral gas (Bahé et al. 2016). Bahé et al. (2017) attributed to this the fact that galaxies in the Hydrangea simulations, a set of resimulations of clusters with the EAGLE physics implementation, show excessive quenching at stellar masses below  $10^{9.5} M_{\odot}$ . In the right panels of Figure 9, we also see enhanced stripping around the locations of newly formed star particles

out to tens of kiloparsecs. Nevertheless, it is still likely that stellar feedback makes some contribution to the effect of ram pressure stripping in the real universe, especially given that compression of gas by ram pressure has been reported to enhance star formation (Vulcani et al. 2018)—an effect also seen in the leading edges of ram pressure stripped galaxies in EAGLE (Troncoso-Iribarren et al. 2020).

Enhanced AGN activity has also been observed in ram pressure stripped galaxies (Peluso et al. 2022), but we do not find this in our sample. This may be because EAGLE is unable to resolve the scales relevant to supermassive black hole feeding and employs simple prescriptions for their accretion. Other simulations suggest that ram pressure can enhance accretion onto the central supermassive black hole (Ricarte et al. 2020; Akerman et al. 2023).

While we find evidence that stellar feedback significantly enhances the stripping rate of gas from galaxies in EAGLE, we find an overall suppression of the stripping rate in the simulation relative to the toy model that increases with ram pressure. As noted above, for gas that is initially ionized but becomes neutral, this can be explained by the fact that the gas is cooling and thus becomes more compact and difficult to strip. This can be seen in the center column of Figure 11, which shows that this type of gas increases in surface mass density between each two simulation outputs at all distances from the galaxy center, an effect not present in the simplified toy model. We note that the increase in gas surface density appears to be

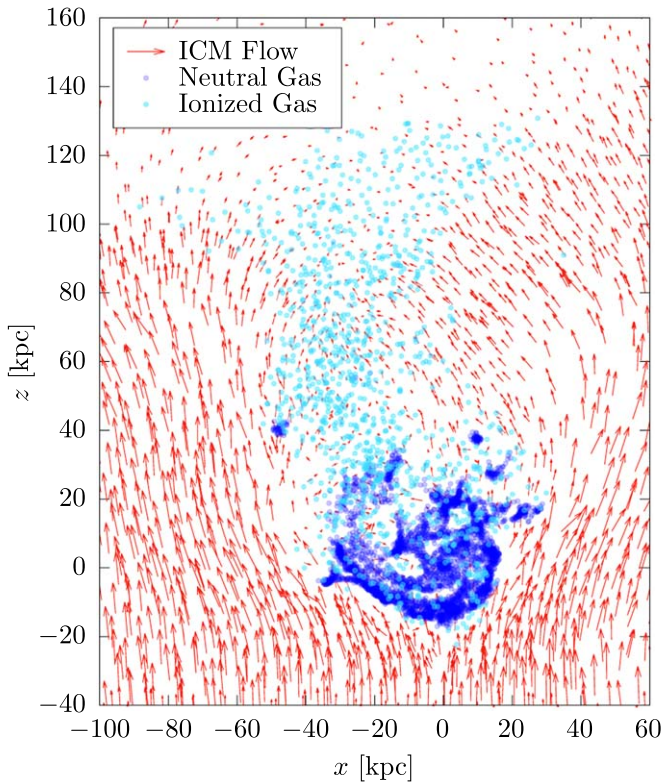


**Figure 12.** The flow of ICM gas particles around a galaxy in our sample. The ICM particles presented are those in a slice between the 10th and 90th percentile  $y$ -axis coordinates of the galaxy gas distribution, where the  $y$ -axis is that perpendicular to the  $x$ - $z$  plane displayed in the figure. The  $z$ -direction is the overall ram pressure direction, computed as described in Section 3.1. Each ICM particle in the slice is plotted as a red arrow proportional to the particle’s velocity in the  $x$ - $z$  plane. The galaxy’s neutral gas is plotted as dark-blue points and the ionized gas as cyan points. It is apparent that the ICM flow is deflected around the galaxy gas.

larger at higher ram pressures, as can be seen in the three bins of increasing ram pressure shown in Figure 11.

However, the toy model also predicts gas mass surface densities that are too low for neutral and ionized gas that do not transition to the other state by the subsequent simulation output. Figure 11 indicates that these types of gas become excessively diffuse in the toy model. This suggests that some confining force that is not present in the simplified toy model acts on the gas. We suggest that this effect may be caused by the deflection of the ICM around the galaxy, creating an inward force and decreasing the total momentum transferred to the galaxy gas in the ram pressure direction. We demonstrate the deflection of the ICM gas around an example galaxy in Figure 12.

## 6. Conclusions

In the previous sections, we compared the evolution of the stripped gas mass fraction of the neutral gas disk and hot ionized halo of galaxies, as predicted by simple analytic models, a more complicated toy model that integrates the motion of gas under ram pressure, and a full hydrodynamical simulation. The analytic models we tested were the formulation from Gunn et al. (1972) for the neutral gas disk and that from McCarthy et al. (2008) for the hot ionized gas halo. The details of these analytic models, and of our toy model, are summarized in Section 3 and Table 2.

The galaxy sample consisted of 80 simulated galaxies across eight clusters at  $z=0$  from the EAGLE simulation, with the evolution of the galaxies being tracked from their entry into the cluster FoFs group. The properties of the galaxies are summarized in Figures 1 and 2 as well as in Table 1.

1. We found that the initial conditions assumed by the McCarthy et al. (2008) model for the gas surface density and maximum gravitational restoring acceleration were in approximate agreement with the true initial surface density from the simulation and the maximum restoring acceleration predicted from kinematically evolving the gas particles in the potential.
2. For the Gunn et al. (1972) model, we found that the maximum gravitational restoring acceleration was significantly underpredicted if taking the gravitational force to come only from the stellar disk, but was much better approximated if accounting for the dark matter by using the same gravitational restoring acceleration as for the McCarthy et al. (2008) model (Figure 3).
3. These analytic models for ram pressure assume that the maximum gravitational restoring acceleration experienced by gas and the gas mass surface density perpendicular to the direction of the ram pressure do not evolve over time. However, this is not the case in a realistic ram pressure stripping situation: the ram pressure changes direction and magnitude as the galaxy moves through the cluster, and the orbits of gas as well as the gas surface density will evolve. We plot this evolution as predicted by our toy model, which takes into account the above factors, in Figure 4. This shows a substantial evolution in the gas surface density within the toy model, with the neutral gas becoming less dense over time and the ionized gas becoming slightly more dense on average, but with substantial scatter among galaxies.
4. The evolution of the gas surface density in the toy model for the ionized gas is reflected in the difference between the toy model and analytic model predictions for the stripping timescales of the ionized gas (Figure 5, panels (b) and (f)). It is also present in the difference between the analytic model and EAGLE simulation in panels (a) and (e), suggesting that it has some true effect.
5. The majority of the difference between the stripping timescales predicted by the analytic models and the simulation is also reflected in the difference between the toy model and the simulation, for both the ionized (Figure 5) and neutral (Figure 6) gas. This suggests that the disparity between the analytic models and the simulation is primarily driven by hydrodynamical and subgrid effects that are present only in the simulation.
6. We identify three main processes in EAGLE that cause the stripping rate to deviate from analytic prescriptions in opposing directions. The gas stripping rate is enhanced by stellar feedback. It is decreased by cooling of the initially ionized gas into denser neutral gas, as well as by a confining force on both the neutral and ionized gas.
7. The excess fraction of gas mass expelled per stellar feedback event (above the prediction for ram pressure stripping alone) increases with increasing ram pressure (Figure 9), implying that ram pressure and feedback work synergistically to expel more gas than would be expected merely from the sum of the two effects.



8. A median of 33% of the gas that is initially in the ionized halo of our galaxies becomes neutral at some point during their evolution (though it may become ionized again later). This enhances the density of the gas in a way that cannot be predicted by simplified models (Figure 11, center column), making it more resistant to stripping.
9. We find that there seems to be a confining force on the gas in our galaxy sample that is stronger at higher ram pressure and leads to the gas being less diffuse than expected from its kinematic initial conditions (Figures 10 and 11).

Overall, while we find that the toy model improves upon the predictions of simple analytic models in limited circumstances (in particular, for the 25% stripping timescale of the ionized halo shown in Figure 5), the results are otherwise similar to those of analytic models when assuming realistic initial conditions for the latter. This suggests that only small improvements can be made to semianalytic models by adopting more complex prescriptions for ram pressure stripping itself.

Instead, the majority of the disparity between the predictions of the EAGLE simulation and those of both the analytic and toy models results from hydrodynamical and subgrid effects. It therefore may be necessary to incorporate prescriptions for such effects in semianalytic models of ram pressure stripping. However, more comparisons between hydrodynamical simulations and observations of ram pressure stripped galaxies are also needed, as different simulations vary in resolution, hydrodynamical scheme, and subgrid prescriptions, and therefore potentially also in their results.

### Acknowledgments

This project has received funding from the European Research Council (ERC) under the European Union’s Horizon 2020 research and innovation program (grant agreement No. 833824).

This work used the DiRAC@Durham facility managed by the Institute for Computational Cosmology on behalf of the STFC DiRAC HPC Facility ([www.dirac.ac.uk](http://www.dirac.ac.uk)). The equipment was funded by BEIS capital funding via STFC capital grants ST/P002293/1, ST/R002371/1 and ST/S002502/1, Durham University and STFC operations grant ST/R000832/1. DiRAC is part of the National e-Infrastructure.

A.I. acknowledges the INAF founding program “Ricerca Fondamentale 2022” (PI A. Iagnesi). R.S. acknowledges financial support from FONDECYT Regular 2023 project No. 1230441.

### Appendix Effect of Tidal Forces

In addition to ram pressure, galaxies in clusters experience tidal interactions with both the central potential of the cluster and other satellite galaxies. A statistical study of these processes in the EAGLE simulation was presented in Marasco et al. (2016). Unlike ram pressure, tidal forces can strip stars and dark matter from galaxies in addition to gas. To limit the number of tidally affected galaxies in our sample, we did not select galaxies that decreased in stellar mass during the EAGLE snapshot in which they entered their host clusters. However, the galaxies are nevertheless able to lose stellar mass during their later evolution. It is also possible for them to lose stellar mass to tidal forces in their outer regions while gaining a larger

amount in their inner regions due to star formation. Furthermore, the ionized gas halo and sometimes the neutral gas disk extend farther out in radius than the stellar distribution, and thus can be affected by tides even if the stars are unaffected. For these reasons, we attempt here to estimate the maximum possible effect of tides on our simulated galaxy sample (Section 2.2).

We exploit the fact that tidal forces, whether from the central galaxy or other satellites, affect stars and dark matter as well as gas. Continuous tidal stripping, such as that typically experienced by a galaxy traveling around the center of a cluster, produces a tidal radius outside of which matter is stripped. This radius should be equal for all types of matter within the galaxy. At each simulation output, we find the dark matter and stellar radii outside of which 90% of the particles of that type become unbound, as long as there are at least 30 particles outside the radius. Defined this way, such a radius does not always exist, particularly for the star particles, because the star particle distribution is less physically extended than the dark matter distribution and thus requires stronger tides to be tidally stripped. We consider the above quantity an estimate of the potential tidal truncation radius.

We would expect this method to fail to estimate the truncation radius of the galaxy gas in cases where the gas extends farther than both the dark matter and the stars, and neither the dark matter nor the stars have a well-defined truncation radius. If the spatial extent of the different particle types is taken to be their 99% radii, then it is only for 4% of the outputs in our sample that the truncation radius is not successfully estimated.

We present the estimated truncation radius in the leftmost panel of Figure A1. In cases where the radius exists for both the dark matter and stars, we plot the two against each other as red squares. Here we see that the estimated truncation radius is generally similar for both types of particles, as would be expected for the tidal radius. Black round points represent galaxies for which the radius exists for the dark matter but not the star particles. For these galaxies, we have instead plotted the truncation radius for the dark matter versus the outer edge of the stellar distribution, represented by the radius of the 30th most distant star particle. The black points show that the edge of the stellar distribution in these galaxies is typically smaller than the truncation radius of the dark matter, as would be expected if the tidal radius is outside the stellar distribution but within the dark matter distribution.

At very small stripping radii, we do see a discrepancy between the tidal radii implied by the stars and those implied by the dark matter. This is because the mechanism of tidal stripping is not always continuous stripping defined by a tidal radius, but is sometimes due to tidal shocks that occur during rapid tidal interactions, such as those between satellite galaxies in the cluster. These interactions unbind matter from the galaxy by increasing its energy. The dark matter is less bound than the stars, and this mechanism therefore strips it to a smaller radius; this has been noted in EAGLE (Jing et al. 2019).

To estimate the amount of stripping if the mechanism is tidal shocks, we repeat the calculation described above for the tidal radius, but instead compute the binding energy per unit mass above which 90% of stellar or dark matter particles are stripped. In the center panel of Figure A1, we plot this value for the dark matter versus the stars as red squares. The simulation outputs at very negative values of the plot correspond to the

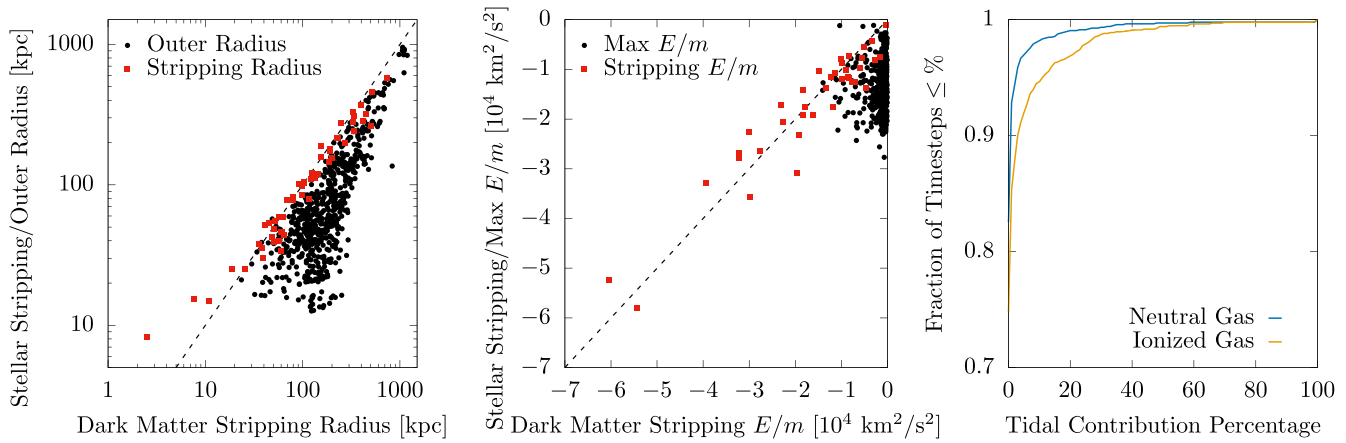


**Figure A1.** Left: the estimated tidal truncation radius of the dark matter, computed as described in the text, vs. the estimated tidal truncation radius of the stars (red squares), or for galaxies in which the latter is nonexistent, the maximum radius of the stellar distribution (black circular points). Center: similar to the left panel, but for the specific binding energy above which particles are tidally unbound, where the black points show the maximum specific binding energy for the stellar distribution. Right: the fraction of simulation outputs having an estimated tidally stripped fraction of gas at or below the percentage given on the horizontal axis. The blue line represents the neutral gas component, and the orange line represents the ionized gas.

points in the left panel at small stripping radii, showing that the energetic increase of the stars and dark matter is similar, but the dark matter is stripped to a smaller radius. As in the left panel, in many galaxies the stars are not stripped, so we plot as black points the limiting specific binding energy of all of the stars, represented by the value for the 30th least bound star particle. We see from this that the stars are typically more bound than the dark matter.

While ram pressure does not directly affect the stars and dark matter as tidal forces do, it indirectly decreases how bound they are by removing gas mass from the subhalo (Smith et al. 2012). Therefore, the stripping parameter estimates shown in the left and center panels of Figure A1 likely overestimate the influence of tides on the stars and dark matter.

Nevertheless, we estimate the fraction of gas that is possibly stripped by tides by taking the maximum of four values: the fraction of gas outside the estimated tidal radius of the dark matter, the fraction of gas with specific binding energy larger than the limiting specific binding energy of the stripped dark matter, and both of the above quantities but for the stars. We present the estimated fraction of neutral and ionized gas stripped by tides in the right panel of Figure A1. This is shown as a cumulative histogram of the fraction of simulation outputs (for all galaxies) that have an estimated tidally stripped mass fraction lower than some percentage. The blue line represents the neutral gas, and the orange line represents the ionized gas. As might be expected, the ionized halo, which is more radially extended and less strongly bound, is more affected by tides than the neutral gas disk. However, for both gas phases, the majority of simulation outputs have little expected influence from tides.

The right panel of Figure A1 shows the *instantaneous* fraction of gas mass we predict to be stripped by tides at each simulation output, but we also compute the expected cumulative fraction of initial gas stripped, as a comparison to the results presented in Figures 5 and 6 in Section 4.3. At the 25% stripping timescale for the neutral gas, we find that the median estimated contribution from tides is 0.35% of the gas mass stripped by that time (i.e., 0.09% of the total neutral gas mass). Six of the 69 galaxies (9%) that reach 25% neutral gas stripping have tidal contributions of over 10% to the mass stripped at that time. At the 75% stripping timescale of the

neutral gas, the median contribution from tides is 1.4%, and three of 48 galaxies (6%) have tidal contributions of over 10%. As expected, the ionized gas is somewhat more influenced by tides: at the 25% stripping timescale, the median tidal contribution is 1.2%, and seven of 79 galaxies (9%) have contributions over 10%. Finally, for the 90% stripping timescale of the ionized gas, the median tidal contribution is 2.2%, and nine of 57 galaxies (16%) have contributions over 10%.

Given the above estimates of the effect of tides on our sample, and especially considering that they are likely to be overestimates, we conclude that the results presented in this paper are not significantly affected by the presence of tides.

### ORCID iDs

Andrea Kulier <https://orcid.org/0000-0002-0431-2445>  
 Bianca Poggianti <https://orcid.org/0000-0001-8751-8360>  
 Stephanie Tonnesen <https://orcid.org/0000-0002-8710-9206>  
 Rory Smith <https://orcid.org/0000-0001-5303-6830>  
 Alessandro Ignesti <https://orcid.org/0000-0003-1581-0092>  
 Nina Akerman <https://orcid.org/0000-0001-7011-9291>  
 Antonino Marasco <https://orcid.org/0000-0002-5655-6054>  
 Benedetta Vulcani <https://orcid.org/0000-0003-0980-1499>  
 Alessia Moretti <https://orcid.org/0000-0002-1688-482X>  
 Anna Wolter <https://orcid.org/0000-0001-5840-9835>

### References

- Akerman, N., Tonnesen, S., Poggianti, B. M., Smith, R., & Marasco, A. 2023, *ApJ*, 948, 18
- Ayromlou, M., Nelson, D., Yates, R. M., Kauffmann, G., & White, S. D. M. 2019, *MNRAS*, 487, 4313
- Bahé, Y. M., Barnes, D. J., Dalla Vecchia, C., et al. 2017, *MNRAS*, 470, 4186
- Bahé, Y. M., Crain, R. A., Kauffmann, G., et al. 2016, *MNRAS*, 456, 1115
- Bahé, Y. M., & McCarthy, I. G. 2015, *MNRAS*, 447, 969
- Bahé, Y. M., McCarthy, I. G., Crain, R. A., & Theuns, T. 2012, *MNRAS*, 424, 1179
- Barnes, D. J., Kay, S. T., Bahé, Y. M., et al. 2017, *MNRAS*, 471, 1088
- Bekki, K. 2009, *MNRAS*, 399, 2221
- Bekki, K., Couch, W. J., & Shioya, Y. 2002, *ApJ*, 577, 651
- Bellhouse, C., McGee, S. L., Smith, R., et al. 2021, *MNRAS*, 500, 1285
- Booth, C. M., & Schaye, J. 2010, *MNRAS*, 405, L1
- Byrd, G., & Valtonen, M. 1990, *ApJ*, 350, 89

- Chabrier, G. 2003, *PASP*, **115**, 763
- Crain, R. A., Bahé, Y. M., Lagos, C. D. P., et al. 2017, *MNRAS*, **464**, 4204
- Crain, R. A., Schaye, J., Bower, R. G., et al. 2015, *MNRAS*, **450**, 1937
- Crain, R. A., Theuns, T., Dalla Vecchia, C., et al. 2009, *MNRAS*, **399**, 1773
- Cullen, L., & Dehnen, W. 2010, *MNRAS*, **408**, 669
- Dalla Vecchia, C., & Schaye, J. 2012, *MNRAS*, **426**, 140
- Davis, M., Efstathiou, G., Frenk, C. S., & White, S. D. M. 1985, *ApJ*, **292**, 371
- Dehnen, W., & Aly, H. 2012, *MNRAS*, **425**, 1068
- Dolag, K., Borgani, S., Murante, G., & Springel, V. 2009, *MNRAS*, **399**, 497
- Dressler, A. 1980, *ApJ*, **236**, 351
- Durier, F., & Dalla Vecchia, C. 2012, *MNRAS*, **419**, 465
- Ferland, G. J., Korista, K. T., Verner, D. A., et al. 1998, *PASP*, **110**, 761
- Franchetto, A., Tonnesen, S., Poggianti, B. M., et al. 2021, *ApJL*, **922**, L6
- Fujita, Y. 2004, *PASJ*, **56**, 29
- Furlong, M., Bower, R. G., Theuns, T., et al. 2015, *MNRAS*, **450**, 4486
- Göller, J., Joshi, G., Rohr, E., Zinger, E., & Pillepich, A. 2023, arXiv:2304.09199
- Gunn, J. E., Gott, J., & Richard, I. 1972, *ApJ*, **176**, 1
- Haardt, F., & Madau, P. 2001, in *Clusters of Galaxies and the High Redshift Universe Observed in X-rays, Recent Results of XMM-Newton and Chandra, XXXVth Rencontres de Moriond, XXIst Moriond Astrophysics Meeting*, ed. D. M. Neumann & J. T. V. Tran (Paris: ARISF)
- Hopkins, P. F. 2013, *MNRAS*, **428**, 2840
- Hough, T., Cora, S. A., Haggard, R., et al. 2023, *MNRAS*, **518**, 2398
- Jáchym, P., Köppen, J., Palouš, J., & Combes, F. 2009, *A&A*, **500**, 693
- Jiang, L., Helly, J. C., Cole, S., & Frenk, C. S. 2014, *MNRAS*, **440**, 2115
- Jing, Y., Wang, C., Li, R., et al. 2019, *MNRAS*, **488**, 3298
- Katsianis, A., Blanc, G., Lagos, C. P., et al. 2017, *MNRAS*, **472**, 919
- Kennicutt, R. C., Jr. 1998, *ApJ*, **498**, 541
- Köppen, J., Jáchym, P., Taylor, R., & Palouš, J. 2018, *MNRAS*, **479**, 4367
- Larson, R. B., Tinsley, B. M., & Caldwell, C. N. 1980, *ApJ*, **237**, 692
- Manuwal, A., Ludlow, A. D., Stevens, A. R. H., Wright, R. J., & Robotham, A. S. G. 2022, *MNRAS*, **510**, 3408
- Marasco, A., Crain, R. A., Schaye, J., et al. 2016, *MNRAS*, **461**, 2630
- McAlpine, S., Helly, J. C., Schaller, M., et al. 2016, *A&C*, **15**, 72
- McCarthy, I. G., Frenk, C. S., Font, A. S., et al. 2008, *MNRAS*, **383**, 593
- Mitchell, P. D., Schaye, J., Bower, R. G., & Crain, R. A. 2020, *MNRAS*, **494**, 3971
- Moore, B., Katz, N., Lake, G., Dressler, A., & Oemler, A. 1996, *Natur*, **379**, 613
- Navarro, J. F., Frenk, C. S., & White, S. D. M. 1996, *ApJ*, **462**, 563
- Pallero, D., Gómez, F. A., Padilla, N. D., et al. 2022, *MNRAS*, **511**, 3210
- Peluso, G., Vulcani, B., Poggianti, B. M., et al. 2022, *ApJ*, **927**, 130
- Pillepich, A., Springel, V., Nelson, D., et al. 2018, *MNRAS*, **473**, 4077
- Planck Collaboration, Ade, P. A. R., Aghanim, N., et al. 2014, *A&A*, **571**, A16
- Poggianti, B. M., Ignesti, A., Gitti, M., et al. 2019, *ApJ*, **887**, 155
- Price, D. J. 2008, *JCoPh*, **227**, 10040
- Qu, Y., Helly, J. C., Bower, R. G., et al. 2017, *MNRAS*, **464**, 1659
- Rahmati, A., Pawlik, A. H., Raičević, M., & Schaye, J. 2013, *MNRAS*, **430**, 2427
- Ramos-Martínez, M., Gómez, G. C., & Pérez-Villegas, Á. 2018, *MNRAS*, **476**, 3781
- Ricarte, A., Tremmel, M., Natarajan, P., & Quinn, T. 2020, *ApJL*, **895**, L8
- Roediger, E., & Brügger, M. 2007, *MNRAS*, **380**, 1399
- Rohr, E., Pillepich, A., Nelson, D., et al. 2023, *MNRAS*, **524**, 3502
- Rosas-Guevara, Y., Bower, R. G., Schaye, J., et al. 2016, *MNRAS*, **462**, 190
- Schaller, M., Dalla Vecchia, C., Schaye, J., et al. 2015, *MNRAS*, **454**, 2277
- Schaye, J. 2004, *ApJ*, **609**, 667
- Schaye, J., Crain, R. A., Bower, R. G., et al. 2015, *MNRAS*, **446**, 521
- Schaye, J., & Dalla Vecchia, C. 2008, *MNRAS*, **383**, 1210
- Schulz, S., & Struck, C. 2001, *MNRAS*, **328**, 185
- Smith, R., Fellhauer, M., & Assmann, P. 2012, *MNRAS*, **420**, 1990
- Springel, V. 2005, *MNRAS*, **364**, 1105
- Springel, V., Di Matteo, T., & Hernquist, L. 2005, *MNRAS*, **361**, 776
- Springel, V., White, S. D. M., Tormen, G., & Kauffmann, G. 2001, *MNRAS*, **328**, 726
- Steinhauser, D., Schindler, S., & Springel, V. 2016, *A&A*, **591**, A51
- Thob, A. C. R., Crain, R. A., McCarthy, I. G., et al. 2019, *MNRAS*, **485**, 972
- Tonnesen, S. 2019, *ApJ*, **874**, 161
- Tonnesen, S., & Bryan, G. L. 2021, *ApJ*, **911**, 68
- Tonnesen, S., Bryan, G. L., & van Gorkom, J. H. 2007, *ApJ*, **671**, 1434
- Troncoso-Iribarren, P., Padilla, N., Santander, C., et al. 2020, *MNRAS*, **497**, 4145
- Vulcani, B., Poggianti, B. M., Gullieuszik, M., et al. 2018, *ApJL*, **866**, L25
- Wendland, H. 1995, *AdCoM*, **4**, 389
- Wiersma, R. P. C., Schaye, J., & Smith, B. D. 2009a, *MNRAS*, **393**, 99
- Wiersma, R. P. C., Schaye, J., Theuns, T., Dalla Vecchia, C., & Tornatore, L. 2009b, *MNRAS*, **399**, 574
- Yun, K., Pillepich, A., Zinger, E., et al. 2019, *MNRAS*, **483**, 1042
- Zinger, E., Joshi, G., Pillepich, A., Rohr, E., & Nelson, D. 2023, arXiv:2304.09202